HHS Public Access

Author manuscript

Neuroimage. Author manuscript; available in PMC 2020 July 01.

Published in final edited form as:

Neuroimage. 2019 July 01; 194: 136–148. doi:10.1016/j.neuroimage.2019.03.044.

Comparative Modeling of Transcranial Magnetic and Electric Stimulation in Mouse, Monkey, and Human

Ivan Alekseichuk[a,*], **Kathleen Mantell**[a], **Sina Shirinpour**[a], and **Alexander Opitz**[a]

[a]Department of Biomedical Engineering, University of Minnesota, Minneapolis, MN, USA

Abstract

Transcranial magnetic stimulation (TMS) and transcranial electric stimulation (TES) are increasingly popular methods to noninvasively affect brain activity. However, their mechanism of action and dose-response characteristics remain under active investigation. Translational studies in animals play a pivotal role in these efforts due to a larger neuroscientific toolset enabled by invasive recordings. In order to translate knowledge gained in animal studies to humans, it is crucial to generate comparable stimulation conditions with respect to the induced electric field in the brain. Here, we conduct a finite element method (FEM) modeling study of TMS and TES electric fields in a mouse, capuchin and macaque monkeys, and a human model. We systematically evaluate the induced electric fields and analyze their relationship to head and brain anatomy. We find that with increasing head size, TMS-induced electric field strength first increases and then decreases according to a two-term exponential function. TES-induced electric field strength strongly decreases from smaller to larger specimen with up to 100× fold differences across species. Our results can serve as a basis to compare and match stimulation parameters across studies in animals and humans.

Keywords

Transcranial magnetic stimulation; Transcranial electric stimulation; Finite element modeling; Animal model; Neuromodulation

1. Introduction

Non-invasive brain stimulation (NIBS) is a promising method to study causality of brain-behavior relationships in humans as well as for clinical research in neurological and psychiatric disorders (Polanía et al., 2018). Two main methods are currently used: transcranial magnetic stimulation (TMS) and transcranial electric stimulation (TES). TMS affects neural tissue by inducing a short-lasting electric field at sub- or suprathreshold intensities via electromagnetic induction (Valero-Cabré et al., 2017). TES generates a long-

*Corresponding authors. Department of Biomedical Engineering, Nils Hasselmo Hall, University of Minnesota, 412 Church St. SE, 55455 Minneapolis, MN, USA. ialeksei@umn.edu (I. Alekseichuk),.

lasting subthreshold electric field that aims to modify spike timing by directly applying electric currents to the scalp (Paulus et al., 2016). On the other end of the intensity spectrum, electroconvulsive therapy (ECT) uses square pulses of high-amplitude electric currents (800–900 mA) to elicit brief seizures (Peterchev et al., 2010). While electric field strength and time course during ECT differ from conventional TES, the relative spatial distribution of electric fields will be identical. Thus, results found for TES will also be relevant for animal models of ECT. The induced electric field in the brain is the main actor for both TMS and TES effects. However, the electric field is also the most difficult feature to predict as it depends not only on controllable factors, such as current intensity and coil or electrode locations, but also on the individual head anatomy and tissue biophysics (Alekseichuk et al., 2018; Datta et al., 2009; Laakso et al., 2015; Miranda et al., 2013; Opitz et al., 2017, 2015, 2011; Peterchev et al., 2012; Thielscher et al., 2011; Wagner et al., 2014).

Stimulation-induced electric fields are difficult to directly assess in humans except in cases of intracranial measurements in surgical epilepsy patients. Thus, modeling approaches are most often used to study NIBS electric field distributions (Miranda et al., 2018). While computational models are clearly useful to guide stimulation protocols and to ensure target engagement (Huang et al., 2017; Opitz et al., 2018, 2016), they still cannot predict the physiological outcome of NIBS studies. This is due to the missing link between the biophysics of stimulation, i.e. electric fields, and the resulting physiological effects. Animal models are crucial to close this knowledge gap because they allow simultaneous measurement of both the biophysics and physiology of NIBS using invasive recordings.

Invasive studies in animal models offer a larger neuroscientific toolset with a higher spatial precision than noninvasive evaluations in humans. Thus, animal work is increasingly used to dissect NIBS mechanisms (Kar et al., 2017; Krause et al., 2017; Vöröslakos et al., 2018). However, the translation of results from the animal literature to humans is challenging because it is unclear how to transfer stimulation parameters and dose regimes to achieve comparable conditions. To date, TES research in small rodents predominantly utilizes currents at 100 to 200 μA peak-to-baseline (Grossman et al., 2017; Liebetanz et al., 2006; Monai et al., 2016; Pedron et al., 2014), while some work uses weaker inputs of 20–100 μA (Faraji et al., 2013; Wachter et al., 2011) or higher than 200 μA (Cambiaghi et al., 2011; Takano et al., 2011). TES in non-human primates typically operates at the intensity of 1–2 mA (Kar et al., 2017; Krause et al., 2017). The same intensity is most common in human studies and clinical applications (Antal et al., 2017; Paulus et al., 2016). For TMS, the stimulation intensities used are in the same range for animal (Hoppenrath and Funke, 2013; Mueller et al., 2014; Pasley et al., 2009) and human studies (Rossi et al., 2009). Further, many animal studies use smaller TMS coils, which result in more focal induced electric fields to compensate for the smaller head size (Deng et al., 2013). There is an implicit assumption that the NIBS dose regimens across species are comparable, yet there is limited evidence and a lack of systematic evaluations.

Here, for the first time, we conduct a systematic comparison of electric fields in the brain during (i) TMS with either a 70 or 25 mm figure-8 coil and (ii) two-electrode TES using realistic FEM models of a mouse, monkey, and human. For both methods, we consider multiple coil/electrode positions and identify relationships between the electric field properties and the properties of the head volume conductor.

2. Materials and methods

2.1. General modeling framework

A realistic whole-body mouse model and head models of a capuchin monkey and a human were created from structural MRI images as described below following the SimNIBS framework (Nielsen et al., 2018; Windhoff et al., 2013). In addition, we generated a range of six-layer spherical models with varying radii to study the effect of head size on NIBS electric fields in a simplified scenario. For all models we simulated electric fields for transcranial magnetic stimulation (TMS) and transcranial electric stimulation (TES). If not stated otherwise, options were set to the SimNIBS 2.1 defaults with the following isotropic conductivities: skin, fat, and muscles as a single soft tissue (σ = 0.465 S/m), bones (σ = 0.01 S/m), eyes (σ = 0.5 S/m), CSF (σ = 1.654 S/m), grey matter (σ = 0.275 S/m), and white matter (σ = 0.126 S/m; not included in the mouse model) (Wagner et al., 2004). Resulting electric fields in the brain (grey matter) were analyzed and compared in MATLAB.

2.2. FEM models

Mouse: We created a FEM model from a segmented individual anatomical atlas of a normal adult male nude mouse "Digimouse" (Dogdas et al., 2007). The atlas was derived from X-ray CT and cryosection images. X-ray CT images were acquired in two bed positions using an Imtek microCAT system (Imtek, Knoxville, TN) and reconstructed with 0.1×0.1×0.1 mm resolution. Cryosections were cut at a thickness of 50 µm with an in-plane resolution of 38.8×38.8 µm. The data were co-registered and resampled on an isotropic 0.1 mm grid. Then, images were segmented for soft tissues, skeleton, and multiple internal organs. Here, we considered the following structures: soft tissues (median thickness around the cranium δ = 1.5 mm), bones (δ = 0.3 mm), eyes, and the whole brain including the cerebellum, medulla, and olfactory bulbs. We manually refined the brain surface to correct remaining small defects and introduced a layer of CSF (δ = 0.1 mm) using FSL (Jenkinson et al., 2012). 3D surfaces were created from the refined atlas using FreeSurfer (Fischl, 2012), and further optimized with MeshFix (Attene, 2010). A tetrahedral based FEM model was generated employing adaptive meshing in Gmsh (Geuzaine and Remacle, 2009) with GM resolved at a higher numerical resolution. The whole-body model comprises ~ 5.8 million tetrahedral elements. The brain volume in the model is 0.38 cm^3, which is the same as the population average (Hammelrath et al., 2016).

Monkey: We used an individual FEM model of a normal adult male capuchin monkey (from Alekseichuk et al., 2018). In short, structural MR imaging (T1 and T2) was performed at the Nathan Kline Institute for Psychiatric Research, USA with approval of the local Institutional Animal Care and Use Committee. Anatomical images were segmented for the soft tissues (δ = 9.4 mm), eyes, skull (δ = 1.3 mm), CSF (δ = 0.6 mm), white and grey matter using Freesurfer and ITKSnap (Yushkevich et al., 2006). Tissue surfaces were created with FreeSurfer and optimized using MeshFix. The FEM head model (~ 4.2 million tetrahedral elements) was generated using Gmsh. The brain volume in the model is 68.31

cm^3, which is very close to the population mean: 68.94 cm^3 for male and 64.32 cm^3 for female specimens (Isler et al., 2008).

We further created an additional FEM model of a macaque head from a macaque anatomical template (Reveley et al., 2016) following the same routine. It comprises ~5.1 million tetrahedral elements with a brain volume of 83.45 cm^3. This is close to the population mean, which is 84.26 cm^3 and 93.71 cm^3 for female and male specimens, respectively (Isler et al., 2008).

Human: We utilized the individual head model of the normal adult male human "Ernie" that is included in SimNIBS 2.1 (Nielsen et al., 2018). T1-weighted and T2-weighted MR images were collected using a 3T scanner (Phillips Achieva™) with a 32-channel head coil at the Copenhagen University Hospital Hvidovre, Denmark. The Ethics Committee of the Capital Region of Denmark approved the MR scans. A T1-weighted contrast was acquired with the following parameters: 3D TFE, TR/TI/TE = 6.9/1000/3.3 ms; TFE factor = 243, 2600ms; flip angle = 8°; 208 sagittal slices; matrix = 256×256; voxel size = 1×1×1 mm^3. T2-weighted image: 3D TSE, TR/TE = 2500/250 ms; flip angle = 90°; 208 sagittal slices; matrix = 244×244; voxel size = 1×1×1 mm^3. The facial region of the images was depersonalized. The following tissues were considered: soft tissues (δ = 8 mm), eyes, skull (δ = 6.9 mm), CSF (δ = 6.6 mm), grey matter, and white matter. The model was generated with the SimNIBS routine 'headreco', which also utilizes Gmsh for adaptive meshing. The final head model comprises ~ 4.2 million tetrahedral elements. The brain volume of 1331.87 cm^3 is in the range of the population distribution: 1273.6 ± 115 cm^3 (mean ± sd) for males and 1131.1±99.5 cm^3 for females (Allen et al., 2002).

Spherical models: We created 13 six-layer spherical models with an outer radius of 0.5 cm, and 1 to 12 cm with 1 cm steps. Each model was linearly scaled from the standard spherical model as included in SimNIBS 2.1 and originally created in Gmsh with the following layers: "ventricles with CSF" (r = 25 mm, σ = 1.654 S/m), "white matter" (r = 75 mm, σ = 0.126 S/m), "grey matter" (r = 80 mm, σ = 0.275 S/m), "CSF" (r = 83 mm, σ = 1.654 S/m), "skull" (r = 89 mm, σ = 0.01 S/m), and "skin" (r = 95 mm, σ = 0.465 S/m). Each model has ~ 480 thousand tetrahedral elements. To ensure that found results for differing radii were not due to differences in tetrahedral element size, we also created high resolution spherical models (~ 8 million elements) for r = 8 to 12 cm.

2.3. Transcranial magnetic stimulation (TMS)

We simulated the electric field for realistic 70 mm and 25 mm figure-8 coils. Both coils have 9 wire loops, and were modeled using the magnetic dipole method as described and validated before (Thielscher and Kammer, 2004, 2002). The coils were positioned over the left central brain region, which corresponds to the primary motor cortex in humans. We simulated three different orientations: 45° to the rostral-caudal axis (towards caudal medial end, anterior-posterior with respect to the motor cortex), 90° to rostral-caudal axis (towards medial end), and −45° to rostral-caudal axis (towards caudal lateral end). The coil center was placed 4 mm above the skin surface. In addition, the rodent specific small bent round coil (conceptually similar to Parthoens et al., 2016) was tested in the mouse model. The coil has

12 wire loops (outer d = 40 mm, two layers), and it allows for only one position over the head due to its shape. The input intensity *dI/dt* was 100 A/μs in every simulation as commonly used in human experiments (Rossi et al., 2009). Overall, 19 simulations (3 FEM models × 3 coil orientations × 2 coil sizes + 1 mouse model with rodent specific coil) were performed using SimNIBS 2.1, which uses the GetDP solver (Geuzaine, 2007).

Using the same parameters, we also investigated the induced electric fields in the 13 six-layer spherical models. Only one coil position was used per sphere due to the spherical symmetry. We further performed a control simulation using high-resolution spheres to ensure that found results are not due to differences in the size of tetrahedral elements.

2.4. Transcranial electric stimulation (TES)

We estimated the electric field for three different two-electrode montages. The montages aimed to maximize the distance between the electrodes on the head within a given anatomical axis to maximize the electric field strength in the brain. The following montages were modeled: 1) Rostral-caudal montage: one electrode over the medial rostral area ("forehead") and another over the medial caudal area ("occiput"). 2) Left-right montage: electrodes over the left and right temporal areas. 3) Dorsalventral montage: one electrode over the left central area ("motor cortex") and another over the right shoulder/neck areas. For the mouse model only, an additional dorsal-abdominal montage was simulated; the electrodes were located over the left central brain area and the central abdominal region. Stimulation electrodes were modeled as 2 mm thick conductive rubber (σ = 29.4 S/m) circles with the diameter scaled according to the head size: 3 mm for the mouse model, 15 mm for the monkey model, and 36 mm for the human model. In addition, for the human model we performed simulations for 3 mm and 15 mm stimulation electrodes. The electric potential was computed using an electrostatic formulation using Dirichlet boundary conditions and solved with the Galerkin method. Boundary conditions were set at the outer surface of the electrodes. The stimulation intensity I was set to 1 mA, in line with the human experimental literature (Antal et al., 2017; Grossman et al., 2018). Overall, 16 simulations (3 FEM models × 3 electrode montages + 1 extra montage for the mouse model + 2 extra electrode sizes for the human model × 3 electrode montages) were performed using SimNIBS 2.1.

Using the same computational pipeline, we also estimated the electric fields for the 13 six-layer spherical models. Two round stimulation electrodes ($r_{electrode} = 0.1 \times r_{sphere}$) were placed on opposite ends of the sphere. In addition, for the "human head size" sphere (r_{sphere} = 10 cm), all electrode sizes with d = 2 to 30 mm were simulated.

2.5. FEM analysis

To quantify the results of TMS and TES simulations, we estimated three main parameters per simulation: robust maximum of the electric field strength (E_{max}), which corresponds to the 99.9th percentile of the electric field strength (the 98th percentile of the electric field strength $E_{98\%}$ is shown in Supplementary Table S2); median of the electric field strength (E_{median}); and affected area, which corresponds to the volume ($L_{½max}$) or surface ($A_{½max}$) where the electric field strength is equal or greater than the half-maximum for the given simulation. We evaluated these parameters in the brain (grey matter) volume and on the brain (grey matter) surface. Tangential and perpendicular/radial components of the induced electric field were separated at the brain surface level and evaluated individually. To estimate the maximum depth of the stimulation ($d_{1/2max}$), we first determined the shortest Euclidian distance between the center of each volume element which is included in $L_{1/2max}$ (affected volume) and the brain surface. Over the elements in this volume we report the maximum depth found. In addition, we estimated the maximum electric field on the scalp surface (E_{max}(scalp)). For TMS, this corresponds to the 99.9th percentile of the electric field strength on the surface. For TES, it is the mean electric field on the scalp surface directly underneath the stimulation electrodes. The ratio of the E_{max} on the scalp to that in the brain is defined as S/B ratio.

We evaluated the relationship between the parameters E_{max}, E_{median}, $L_{½max}$, $A_{½max}$ and the total head volume in both the anatomically realistic and spherical FEM models using the MATLAB Curve Fitting Toolbox. We considered a set of plausible functions employing the Levenberg-Marquardt algorithm with a robust nonlinear least squares fitting method. Goodness-of-fit metric, namely adjusted R-squared (R^2_{adj}), is reported for the identified best fit.

The data and code for data analysis are available from the corresponding authors upon reasonable request.

3. Results

3.1. Transcranial magnetic stimulation (TMS)

TMS-induced electric fields were simulated for three coil positions and two coil sizes (70 mm and 25 mm figure-8 coils) in the mouse, capuchin monkey, and human FEM models. All simulations were performed for the same input intensity *dI/dt* of 100 A/μs. Resulting electric field strengths in grey matter are highly comparable between coil positions (Fig. 2A, B), but vary substantially for different coil sizes and head models (Tables A1, A2).

For the 70 mm figure-8 coil, the average robust maximum electric field (E_{max}) across the grey matter volume is 56.6 mV/mm for the mouse, 126.4 mV/mm for the monkey, and 126.8 mV/mm for the human. Thus, the cross-species ratio of E_{max} is 0.45:1:1. The distribution of the electric field on the brain surface across species is shown in Fig. 2C (for other coil positions see Fig. S1, S2). The relative volume of stimulation ($L_{½max}$) also varies by an order of the magnitude: on average 35.8% of brain volume in the mouse, 8.8% in the monkey, and 2.3% in the human is affected (ratio 15.57:3.83:1). The stimulation depth ($d_{1/2max}$) is on average 2.55 mm in the mouse, which constitutes 54.28% of the distance from the brain surface to its center, 4.79 mm in the monkey (20.04%), and 4.25 mm in the human model (6.36%).

For the 25 mm figure-8 coil, the grey matter volume average E_{max} is 81.3 mV/mm, 113.4 mV/mm, and 86.5 mV/mm for mouse, monkey, and human, respectively (ratio 0.94:1.31:1). These values are comparable between the mouse and human models, but higher in the monkey model. Average $L_{½max}$ is 33.5%, 6%, and 1.3% for mouse, monkey, and human, respectively (ratio 25.77:4.62:1). Average $d_{1/2max}$ is 2.51 mm (53.56% of the distance from the brain surface to the center) in the mouse, 4.53 mm (18.97%) in the monkey, and 4.06 mm (6.07%) in the human.

Comparing the small 25 mm to the standard 70 mm figure-8 coil, mean E_{max} in the brain is higher in the mouse (81.29 vs 56.59 mV/mm), yet lower in the monkey (113.36 vs 126.44 mV/mm) and the human (86.47 vs 126.76 mV/mm). Mean $L_{½max}$ is comparable between the coils in the mouse (33.46 vs 35.79%), but in the monkey and human $L_{½max}$ is lower for the 25 mm coil (monkey: 6.05 vs 8.76%; human: 1.3 vs 2.28%). The stimulation depth ($d_{1/2max}$) is marginally higher for the 70 mm vs 25 mm figure-8 coil: 54.28% vs 53.56% in the mouse, 20.04% vs 18.97% in the monkey, and 6.36% vs 6.07% in the human model. This depth-focality trade-off with more focal but less deep fields for smaller TMS coils has been reported before in the literature (Deng et al., 2013).

Considering that the physiological effects of the electric field depend on its orientation in the brain (Balslev et al., 2007; Brasil-Neto et al., 1992; Opitz et al., 2013; Richter et al., 2013), we separated the electric field into tangential and perpendicular components (Fig. 3 and Tables A1, A2). We then further analyzed the spatial distributions of tangential and perpendicular components.

On average, for the 70 mm figure-8 coil, the ratio of the median magnitude (E_{median}) of the tangential and perpendicular field components is 2.86, 1.79, and 1.72 in mouse, monkey, and human, respectively. These ratios relate to each other as 1.66:1.04:1. The same pattern exists for the 25 mm figure-8 coil: the ratio of E_{median} of the tangential to perpendicular components is 2.75, 1.77, and 1.71 in mouse, monkey, and human, respectively (relate as 1.61:1.04:1).

A summary of all data is depicted in Figure 4A–C. As shown above, TMS-induced electric fields in the brain are getting stronger from the mouse to monkey and human for the 70 mm figure-8 coil. For the 25 mm figure-8 coil, first an increase from mouse to monkey is visible and then a decrease from monkey to human. Regarding relative affected volume $L_{½max}$, it decreases from mouse to monkey to human for both coil sizes.

To analyze how brain/head size affects the electric fields in a simplified model, we computed the TMS-induced electric field in ideal six-layer spherical models of different sizes (r = 0.5 to 12 cm). This size range includes approximations of animal models, such as small rodents (r = 0.5–1 cm) and non-human primates (r = 4–6 cm), and humans (r = 9–11 cm). Here, we found a two-term exponential relationship between the electric field strength and head dimensions: E_{max} first increases and later decreases with increasing head size ($R^2_{adj} \approx 1$; Fig. S6A). We confirmed that the found results are not due to differences in the size of tetrahedral elements by re-running the simulations for the large spheres at higher resolution.

Further, given the complex relationship of the electric field strength and brain volume in our numerical simulations, we independently implemented an analytical approach. For this, we calculated the induced electric field in a spherical model for the figure-8 coils using an analytical formulation (originally derived by Eaton, 1992; further details in Appendix B). Our analytical approach also arrives at a two-term exponential relationship between the electric field and brain size (Fig. S6B) with first increasing and then decreasing field strength. Importantly, this relationship is preserved even after disregarding the factor of coil-to-brain distance, which otherwise increases with the overall head dimensions. To examine this, we simulated a single-layer spherical model where the distance between the TMS coil and the volume of interest is kept identical for every sphere size (Fig. S7). The figure still shows a two-term exponential relationship.

With increasing head volume, the TMS-induced electric field in the brain first gets stronger and then weaker following an exponential function. The inflection point occurs earlier for a smaller, 25 mm figure-8 coil than for the bigger 70 mm figure-8 coil. For the latter, both monkey and human head sizes are near the peak of the function.

A specialized TMS coil design for rodents was previously suggested to match the properties of the induced electric field closer to the human case (Fig. S5). Here we considered one prominent example which is the application of a small circular TMS coil (d = 40 mm) with a slight bent around the rodent's head (following Parthoens et al., 2016). The affected volume $L_{½max}$ of 21.59% is smaller than for the 70 mm or 25 mm figure-8 coils in the mouse (35.8% and 33.5%, respectively), albeit still much larger than for the standard 70 mm figure-8 coil in the monkey and human head models (8.8% and 2.3%). In addition, the ratio of the median magnitude of the tangential to perpendicular field components of 11.44 indicates a strong prevalence of the tangential field, differing to the monkey or human cases.

Another question we examined is the electric field strength on the scalp and its ratio to E_{max} in the brain (Table S1). We found that, on average, TMS with a 70 mm figure-8 coil induces up to 135.99, 222.14, and 278.42 mV/mm on the scalp surface in the mouse, monkey, and human model, respectively. These values are 2.41, 1.76, and 2.2 times higher than in the brain. TMS with a 25 mm figure-8 coil generates up to 179.6, 217.23, and 306.08 mV/mm on the scalp, which is 2.21, 1.92, and 3.54 times higher than in the brain.

3.2. Transcranial electric stimulation (TES)

We modeled TES for three two-electrode montages in a mouse, capuchin monkey, and human model. The stimulation intensity was set to the same level of 1 mA for every simulation. We further modelled an additional electrode montage specific for rodent studies with one electrode located over the head and one over the abdominal area. The results for this montage are highly similar to the dorsal-ventral montage, so it was not included in the group statistics below. All results are shown in Tables A3 and A4.

First, we compared electric fields across electrode montages. Here we found that the robust electric field strength maximum (E_{max}) in the brain shows a wide disparity between montages: 34.98, 20.24, and 52.18 mV/mm for the mouse (mean = 35.8 mV/mm); 0.85, 1.32, and 1.06 for the monkey (mean = 1.08 mV/mm); and 0.3, 0.35, and 0.22 for the human model (mean = 0.29 mV/mm). Average ratio across species is 123.45:3.72:1 (see Fig. 5 and Fig S3).

Considering the relative brain volume of stimulation ($L_{½max}$), we found 25.23%, 69.91%, and 9.93% for the mouse (mean = 35.02%); 41%, 17.15%, 21.1% for the monkey (mean =

26.42%), and 5.58%, 7.23%, and 29.21% for the human (mean = 14%). The ratio of these values is 2.5:1.89:1. Noticeably, there is high variability between the different electrode montages. At the same time, the stimulation depth $d_{1/2max}$ is more consistent across the montages and on average 2.48 mm for the mouse (52.7% of the maximum depth), 5.63 mm (23.57%) for the monkey, and 16.07 mm (24.06%) for the human model.

The maximum electric field strength on the scalp is, on average, 254.49, 9.04, and 2.05 mV/mm for the mouse, monkey, and human (Table S1). These numbers are 8.13, 8.77, and 7.28 times higher than in the brain.

In addition, we evaluated the tangential and perpendicular components of the electric field in a separate analysis (Fig. 6). It was demonstrated using multi-scale models that the orientation of the electric field can have different effects on neurons (Seo and Jun, 2019). Thus, the ratio between tangential and perpendicular electric fields might be an important factor for translational studies in animal models. The ratios of the median magnitude (E_{median}) of the tangential to perpendicular electric field components are 3.89, 3.42, and 1.92 in the mouse (mean = 3.08); 1.63, 1.64, and 1.42 in the monkey (mean = 1.56); 2, 1.5, and 1.5 in the human (mean = 1.67). Mean values relate as 1.84:0.93:1. These values are similar if we consider E_{max} instead of E_{median} of the tangential to perpendicular electric field components (Supplementary Table S3).

The summary of all TES data is shown in Figure 4D–F. Unlike TMS, E_{max} estimates for TES are decreasing from smaller to larger organisms. At the same time, the relative affected volume $L_{½max}$ varies greatly due to the large variability across electrode montages.

We also simulated TES electric fields in ideal spherical head models. We simulated 13 six-layer spheres with radii r = 0.5 cm and from 1 to 12 cm with two electrodes attached on opposite sites (Fig. S6A). We found that the maximum electric field strength E_{max} exponentially decreased with increasing radius ($R^2_{adj} \approx 1$).

Considering the differences in TES applications across animal and human studies, one apparent distinction is the electrode sizes. Naturally, electrodes to be used for mouse stimulation are much smaller than for those in humans. Here, we simulated round electrodes with d = 3 mm for the mouse, 15 mm for the monkey, and 36 mm in humans. Given the same stimulation intensity I of 1 mA, the ratio of current to surface area I/A at the electrode-skin interface was 140.85, 5.65, and 0.98 A/m^2, respectively. To investigate the role of different electrode sizes, we conducted an additional series of simulations in the human head model using all three above-mentioned electrode sizes (Table A4). For the left-right electrode montage, the maximum electric field E_{max} in the grey matter volume had only a weak dependency of the I/A ratio: E_{max} = 0.43, 0.40, and 0.35 mV/mm for I/A = 140.85, 5.65, and 0.98 A/m^2, respectively (Fig. 7B, linear R^2_{adj} = 0.29), with slightly higher fields for a smaller surface area. The two other montages, rostral-caudal and dorsal-ventral, did not show such a trend (Fig. 7A, C). We further evaluated the effect of I/A ratio in the spherical model with r = 10 cm and stimulation electrodes size ranging from d = 2 to 30 mm (Fig. S8B, C). We found a significant linear decrease in E_{max} with increasing electrode size (R^2_{adj} = 0.89, slope β_1 = −0.004). However, the slope of the regression is small with values ranging from 0.234 mV/mm for 2 mm electrodes to 0.184 mV/mm (−21.37%) for 30 mm electrodes. Altogether, the difference in electrode sizes for mouse, monkey, and human had only a small effect on the found results.

4. Discussion

Here, we systematically evaluated the TMS- and TES-induced electric fields in realistic mouse, monkey, and human FEM models. We directly compared electric fields for matched stimulation conditions across species.

There are several key findings regarding TMS: (i) the electric field strength first increases with increasing head size and then decreases; (ii) the inflection point of this function depends on the coil size with the smaller coil showing a decrease in electric field strength starting at a smaller head size; (iii) the relative affected brain volume and stimulation depth decrease with head size; (iv) the tangential electric field component dominates the perpendicular component across all species, but more so in the mouse model. For the 70 mm figure-8 coil, the maximum induced electric field is 55% lower in the mouse than in the monkey and human, where the field strengths are comparable. The use of a smaller 25 mm figure-8 coil leads to comparable electric fields in the mouse and human, but 30% stronger electric field in the monkey. Both coils affect a smaller relative brain volume in the human in comparison to the monkey (~ 4-times) and mouse (~ 20-times).

Analyzing TMS-induced electric fields in anatomically realistic and simplified spherical models, we found an increase in electric field strength with head size which was reversed to a decrease for even larger radii. A possible mechanism for this effect is that the head underneath the TMS coil captures a fraction of the total magnetic flux. This fraction increases with increasing head size; thus, the induced electric field gets stronger (Weissman et al., 1992). However, once the head reaches a certain dimension relative to the coil size, the captured energy is maximized, but the induced electric current is spread through a larger conductive volume and thus creates a weaker electric field. For a smaller TMS coil, the maximum magnetic flux captured occurs at a smaller head volume, which results in an earlier decrease. The function of the induced electric field with increasing head size should reach an asymptote for much larger head sizes relative to the TMS coil (e.g. for micro coils) where the exact head size will not matter anymore, and coil characteristics will dominate the behavior.

Our key findings for TES are: (i) the electric field strength in the brain decreases with increasing head size; (ii) the electric field strength and affected brain volume strongly vary with the electrode montage; (iii) the tangential field is larger than the perpendicular component in all models, but more so in the mouse. We attribute the strong decrease of the TES electric field with increasing head size, which is notably opposite to the relationship found in TMS, to progressively thicker layers of tissues around the brain and thus increasingly diluted current density. The poorly conducting skull isolates the brain, while highly conductive soft tissues and CSF provide avenues for current shunting. This resulted in up to 100-times higher electric fields in the mouse model compared to the human model for the same stimulation intensity. Electric fields in the monkey model were found to be ~ 3-

times higher than in the human. On average, the stimulation affects a 1.9-times larger brain volume in the monkey and a 2.5-times larger relative brain volume in the mouse than in the human. Of note is the high variability of electric field strengths for different electrode montages, as was already demonstrated before for non-human primates (Alekseichuk et al., 2018; Opitz et al., 2016). To demonstrate that the present findings are representative, we created another head model from a macaque anatomical template (Reveley et al., 2016). On average, across three electrode montages, we found electric field strengths similar to our other monkey model (Fig. S9): E_{max} = 1.13 mV/mm (compared to 1.08 mV/mm reported above) and E_{median} = 0.49 mV/mm (compared to 0.42 mV/mm). Nevertheless, for every given experiment, it will be important to consider both the electrode montage and individual anatomy.

Both TMS and TES simulations indicate that specific properties of the induced electric fields in the human brain are better captured in monkeys than in mice. Besides a more comparable electric field strength in the brain and affected brain volume, the ratio of tangential to perpendicular electric field components is similar in human and monkey models. In the mouse, the tangential field component dominates (~ 60–80% higher) in the brain both during TMS and TES, albeit for the latter modality the results are more variable across electrode montages. The prevailing tangential component is due to the lack of gyrification in a lissencephalic rodent in contrast to a gyrencephalic primate. While the electric field strength can be easily scaled (within safety limits) by adjusting the TMS or TES intensity, the ratio of electric field components cannot. However, the implications of these different electric field components on the resulting physiological effects are less clear. It is known that the electric field predominantly affects neural cells that are oriented parallel to the electric field (Aspart et al., 2018; Radman et al., 2009; Rawji et al., 2018; Terzuolo and Bullock, 1956), and a critical mass of affected neurons is necessary to elicit a system-level response. The dissimilar balance of tangential to perpendicular electric field components in the mouse brain could change the system-level response to NIBS relative to the human. Although this is speculative, research in non-human primates should remain essential for understanding the mechanisms of brain stimulation.

The maximum depth of the affected brain volume is lower for the mouse in absolute terms (≈ 2.5 mm for both TES and TMS) compared to the monkey (≈ 4–6 mm) and human (≈ 4–5 mm for TMS, and ≈ 16 mm for TES). However, one should consider these results in relation to the physical brain size of the specimen. The stimulation depth found in the mouse model constitutes 50–60% of the distance between the brain surface and the center of the mouse brain, which arguably reaches deep brain structures. For TMS, the deepest affected elements are about 20% deep in the monkey brain and 6% deep in the human brain. For TES, the deepest affected elements are approx. 20–25% deep in both the monkey and human. Importantly, these results are independent from the stimulation waveform. Thus, transcranial deep brain stimulation (e.g., Grossman et al., 2017) likely requires different approaches in rodents than in humans or non-human primates.

The ratio of electric fields on the scalp and in the brain can be important to determine the amount of peripheral to central nervous system stimulation (Liu et al., 2018). Here, we found TMS electric fields to be ~ 2 times stronger on the scalp level and TES electric fields

~ 8 times stronger than in the brain. These ratios were found to be comparable across species.

In this study, we provide a comprehensive evaluation of TMS and TES electric fields across different species. Our results validate and significantly expand on previous modeling efforts. One earlier study investigated the TMS-induced electric field with respect to brain size using spherical models (Weissman et al., 1992). It demonstrated a steady up to 5-times increase in the induced electric field magnitude as a function of increasing model radius from 0.5 to 7.5 cm, which agrees with our results for the given size range and a large coil. We also confirm a broad TMS-induced electric field in the mouse brain, which is qualitatively different from the one in humans (Crowther et al., 2014; Salvador and Miranda, 2009). While using a smaller TMS coil reduces the relative stimulation volume in rodents, it is still much larger than in humans. Intracranial application of short-pulsed electric currents might be a way to mimic the TMS-induced electric field in a mouse in a realistic manner (Barnes et al., 2014). Electric fields in humans and monkeys due to TMS using a standard 70 mm figure-8 coil are largely similar. An important caveat is that this was shown here with one specific human and monkey model and can slightly differ for other individuals in a given experiment.

A previous modelling study of TES in a mouse with a bihemispheric electrode montage showed a maximum electric field strength of ~ 20 mV/mm per 1 mA in the brain (Bernabei et al., 2014), which is in good agreement with our results. This led researchers to assume a ratio of 50:1 in the TES electric field in mouse relative to humans, where we would expect a maximum field strength of ~ 0.4 mV/mm (Huang et al., 2017; Opitz et al., 2016). However, we demonstrate that other electrode montages can create stronger electric fields, up to 50 mV/mm. On average, our estimate of electric field strengths in a mouse model roughly relate to those in human as 100:1. Thus, a typical TES intensity of 1–2 mA in humans (Antal et al., 2017; Paulus et al., 2016) approximately translates to mice as 10–20 μA and monkeys as 0.3–0.6 mA. Commonly used intensities of 0.1 mA and higher in previous studies in mice (e.g., Grossman et al., 2017; Monai et al., 2016) lead to electric field strengths that are way above what is safe and tolerable in human application (Nitsche and Bikson, 2017). Importantly, TES electric fields in animals and humans strongly depend on the specific electrode montage and individual anatomy. Thus, precise measurements and simulations for every specific case can improve the reliability and transferability of results. Nevertheless, our modeling results of intracranial electric fields are in good agreement with existing *in vivo* measurements in monkeys and humans (Alekseichuk et al., 2018; Huang et al., 2017; Opitz et al., 2018, 2016). Future developments including the combination of FEM electric field modeling with realistic neuron models (Seo and Jun, 2019, 2017; Aberra et al., 2018) can lead to further insights into interspecies differences with respect to their response to TMS and TES.

In conclusion, we provide a systematic evaluation of TES- and TMS-induced electric fields in two popular animal models and compare them to the human case. We outline differences and similarities between electric fields across species and draw attention to the effects of head/brain size and brain gyrification. Notably TMS and TES differ in their relationship of electric field strength and head size in almost an opposite manner. To generate the same intracranial electric field strength in a mouse as in a human using comparable coil or electrode configurations, TMS intensity should typically be *higher*, yet TES intensity should be two orders of magnitude *lower*. For a monkey, our data advocate the use of the *same* TMS intensity and three times *lower* TES intensity to what is applicable in humans. However, while we provide general guidelines for scaling TMS and TES stimulation parameters across species, significant variability in the electric field strength across individuals and stimulation montages stresses the importance of exact estimations for every experiment and individual participant.

Supplementary Material

Refer to Web version on PubMed Central for supplementary material.

Acknowledgments

This work was supported by the University of Minnesota's MnDRIVE Initiative, the Institute for Engineering in Medicine at the University of Minnesota, and NIH grant R01MH118930.

Appendix A.: Data tables

Table A1.

Summary of TMS modeling results (70 mm figure-8 coil). The following coil orientations targeting the left central brain area ("motor cortex") were simulated for the mouse, monkey, and human models: caudal-medial (CM), medial (M), and caudal-lateral (CL). The affected area is defined as the volume ($L_{½max}$) or surface ($A_{½max}$) where the electric field strength is equal or greater than the half-maximum for a given simulation. The stimulation depth $d_{1/2max}$ indicates the deepest point of the affected volume $L_{½max}$ as an absolute (in mm) and relative distance (% of the distance from the brain surface to the brain center). The robust maximum E_{max} corresponds to the 99.9 percentile of the simulated electric field strength in the volume or on the surface.

TMS	Mouse			Capuchin Monkey			Human		
	CM	M	CL	CM	M	CL	CM	M	CL
Grey Matter Volume									
E_{max}, mV/mm	59.13	51.62	59.01	128.35	125.59	125.38	124.58	123.37	132.33
E_{median}, mV/mm	26.16	20.49	23.57	28.83	24.13	25.84	11.61	10.34	11.43
$L_{½max}$, %	40.97	32.67	33.72	8.65	8.12	9.50	2.00	2.66	2.19
$d_{1/2max}$, mm	2.66	2.41	2.58	4.06	4.91	5.4	4.25	4.25	4.25
$d_{1/2max}$, %	56.66	51.19	55.00	16.98	20.56	22.57	6.36	6.36	6.36
Grey Matter Surface									
E_{max}, mV/mm	62.46	53.18	60.42	144.21	138.73	134.39	134.22	133.09	139.82
E_{median}, mV/mm	26.31	21.08	23.84	27.18	22.00	24.14	12.70	11.75	12.62
$A_{½max}$, %	40.60	37.03	37.93	6.63	6.59	8.37	1.93	2.58	2.21
Grey Matter Surface – Tangential Component									
E_{max}, mV/mm	60.20	52.40	59.82	142.12	134.78	130.30	123.87	123.56	132.68
E_{median}, mV/mm	22.88	17.56	21.24	19.31	16.07	18.99	9.47	8.50	9.46

TMS	Mouse			Capuchin Monkey			Human		
	CM	M	CL	CM	M	CL	CM	M	CL
$A_{½max}$, %	37.11	32.10	32.78	4.85	4.67	6.45	1.36	2.00	1.68
Grey Matter Surface – Perpendicular Component									
E_{max}, mV/mm	32.37	28.53	33.73	99.35	100.48	100.10	85.74	83.37	84.19
E_{median}, mV/mm	7.42	6.98	7.13	11.32	9.77	9.36	5.73	4.86	5.39
$A_{½max}$, %	0.25	0.25	0.20	0.82	0.91	0.97	0.45	0.47	0.32

Table A2.

Summary of TMS modeling results (25 mm figure-8 coil). The following coil orientations targeting the left central brain area ("motor cortex") were simulated for the mouse, monkey, and human models: caudal-medial (CM), medial (M), and caudal-lateral (CL). The affected area is defined as the volume ($L_{½max}$) or surface ($A_{½max}$) where the electric field strength is equal or greater than the half-maximum for a given simulation. The stimulation depth $d_{1/2max}$ indicates the deepest point of the affected volume $L_{½max}$ as an absolute (in mm) and relative distance (% of the distance from the brain surface to the brain center). The robust maximum E_{max} corresponds to the 99.9 percentile of the simulated electric field strength in the volume or on the surface.

TMS	Mouse			Capuchin Monkey			Human		
	CM	M	CL	CM	M	CL	CM	M	CL
Grey Matter Volume									
E_{max}, mV/mm	84.24	75.38	84.25	118.43	113.12	108.53	83.88	84.22	91.31
E_{median}, mV/mm	35.66	29.10	32.24	20.57	17.32	17.85	4.34	3.78	4.20
$L_{½max}$, %	37.99	30.82	31.57	5.84	5.64	6.66	1.28	1.52	1.09
$d_{1/2max}$, mm	2.58	2.38	2.58	3.85	4.57	5.18	4.21	4.28	3.68
$d_{1/2max}$, %	55.00	50.69	55.00	16.12	19.12	21.68	6.31	6.41	5.50
Grey Matter Surface									
E_{max}, mV/mm	89.39	77.81	85.74	134.53	126.72	119.25	94.25	96.28	99.93
E_{median}, mV/mm	35.68	29.77	32.23	19.57	16.18	16.59	4.78	4.33	4.63
$A_{½max}$, %	37.66	34.58	36.14	4.46	4.69	5.91	1.16	1.34	1.10
Grey Matter Surface – Tangential Component									
E_{max}, mV/mm	85.96	76.66	85.35	131.80	122.42	114.84	85.64	87.54	94.54
E_{median}, mV/mm	30.80	24.20	28.65	13.63	11.86	12.59	3.58	3.13	3.51
$A_{½max}$, %	35.16	30.33	31.01	3.36	3.53	4.94	0.88	1.08	0.80
Grey Matter Surface – Perpendicular Component									
E_{max}, mV/mm	45.32	40.60	46.74	90.30	84.37	81.44	56.64	55.75	56.11
E_{median}, mV/mm	10.22	10.23	9.94	8.33	6.74	6.39	2.17	1.79	2.03
$A_{½max}$, %	0.19	0.19	0.16	0.63	0.61	0.57	0.28	0.24	0.21

Table A3.

Summary of TES modeling results. The following montages were simulated for the mouse, capuchin monkey, and human model: rostral-caudal (R-C), left-right (L-R), and dorsal-ventral (D-V). In addition, a dorsal-abdominal (D-A) montage is included for the mouse model. The affected area is defined as the volume ($L_{½max}$) or surface ($A_{½max}$) where the electric field strength is equal or greater than the half-maximum for a given simulation. The stimulation depth $d_{1/2max}$ indicates the deepest point of the affected volume $L_{½max}$ as an absolute (in mm) and relative distance (% of the distance from the brain surface to the brain center). The robust maximum E_{max} corresponds to the 99.9 percentile of the simulated electric field strength in the volume or on the surface.

TES	Mouse				Capuchin Monkey			Human		
	R-C	L-R	D-V	D-A	R-C	L-R	D-V	R-C	L-R	D-V
Grey Matter Volume										
E_{max}, mV/mm	34.98	20.24	52.18	51.81	0.85	1.32	1.06	0.30	0.35	0.22
E_{median}, mV/mm	15.87	12.52	14.21	15.14	0.41	0.48	0.38	0.10	0.09	0.09
$L_{½max}$, %	25.23	69.91	9.93	9.95	41.00	17.15	21.10	5.58	7.23	29.21
$d_{1/2max}$, mm	2.58	2.78	2.07	2.12	6.05	5.45	5.40	15.69	15.22	17.31
$d_{1/2max}$, %	54.9	59.22	44.00	45.18	25.30	22.79	22.61	23.49	22.78	25.91
Grey Matter Surface										
E_{max}, mV/mm	37.35	21.00	53.70	53.04	0.87	1.44	1.09	0.30	0.38	0.22
E_{median}, mV/mm	15.47	11.99	12.78	13.96	0.41	0.46	0.36	0.10	0.08	0.08
$A_{½max}$, %	24.00	61.03	11.96	12.09	38.46	11.39	15.08	7.30	5.09	20.73
Grey Matter Surface - Tangential Component										
E_{max}, mV/mm	36.75	17.42	34.50	38.06	0.77	1.30	0.96	0.26	0.32	0.20
E_{median}, mV/mm	14.33	9.43	10.74	12.36	0.31	0.36	0.27	0.08	0.06	0.06
$A_{½max}$, %	17.08	41.82	3.98	4.52	28.57	5.54	8.95	7.06	4.26	12.38
Grey Matter Surface – Perpendicular Component										
E_{max}, mV/mm	26.24	20.30	52.93	52.15	0.78	1.24	0.96	0.23	0.31	0.17
E_{median}, mV/mm	3.68	2.76	5.60	5.42	0.19	0.22	0.19	0.04	0.04	0.04
$A_{½max}$, %	1.74	14.77	4.91	4.91	10.24	5.58	7.11	2.33	2.29	5.33

Table A4.

Summary of TES modeling. The following two-electrode montages with variable electrode sizes are estimated for the human model: rostral-caudal (R-C), left-right (L-R), and dorsal-ventral (D-V). The affected area is defined as the volume ($L_{½max}$) or surface ($A_{½max}$) where the electric field strength is equal or greater than the half-maximum for a given simulation. The stimulation depth $d_{1/2max}$ indicates the deepest point of the affected volume $L_{½max}$ as an absolute (in mm) and relative distance (% of the distance from the brain surface to the brain center). The robust maximum E_{max} corresponds to the 99.9 percentile of the simulated electric field strength in the volume or on the surface.

TES	Electrode d = 36 mm			Electrode d = 15 mm			Electrode d = 3 mm		
	R-C	**L-R**	**D-V**	**R-C**	**L-R**	**D-V**	**R-C**	**L-R**	**D-V**
Grey Matter Volume									
E_{max}, mV/mm	0.30	0.35	0.22	0.32	0.40	0.21	0.31	0.43	0.22
E_{median}, mV/mm	0.10	0.09	0.09	0.10	0.09	0.09	0.09	0.09	0.09
$L_{½max}$, %	5.58	7.23	29.21	3.53	5.28	29.57	3.30	4.77	29.70
$d_{1/2max}$, mm	15.69	15.22	17.31	15.52	14.42	17.31	14.53	11.83	17.31
$d_{1/2max}$, %	23.49	22.78	25.91	23.23	21.58	25.91	21.75	17.71	25.91
Grey Matter Surface									
E_{max}, mV/mm	0.30	0.38	0.22	0.32	0.44	0.21	0.31	0.46	0.22
E_{median}, mV/mm	0.10	0.08	0.08	0.10	0.08	0.08	0.09	0.09	0.08
$A_{½max}$, %	7.30	5.09	20.73	5.03	3.62	21.16	4.78	3.34	21.25
Grey Matter Surface – Tangential Component									
E_{max}, mV/mm	0.26	0.32	0.20	0.27	0.37	0.20	0.26	0.39	0.20
E_{median}, mV/mm	0.08	0.06	0.06	0.08	0.07	0.06	0.08	0.07	0.06
$A_{½max}$, %	7.06	4.26	12.38	5.34	3.00	12.73	5.09	2.78	12.85
Grey Matter Surface - Perpendicular Component									
E_{max}, mV/mm	0.23	0.31	0.17	0.24	0.35	0.17	0.24	0.37	0.17
E_{median}, mV/mm	0.04	0.04	0.04	0.04	0.04	0.04	0.04	0.04	0.04
$A_{½max}$, %	2.33	2.29	5.33	1.93	1.63	5.44	1.87	1.52	5.47

Appendix B.: Analytical formulation of TMS-induced electric field

The analytical solution of the TMS-induced electric field follows the method by Eaton derived for a homogeneous spherical volume conductor for an arbitrary TMS coil geometry (Eaton, 1992). Below we summarize the essential equations and their derivation for one wire loop figure-8 coil. To simplify the equations, the origin of the spherical coordinate system is set as the center of the model. Time varying signals have the form $e^{j\omega t}$, where $j = \sqrt{-1}$ and ω is the angular frequency. The electric field $\boldsymbol{E}$ first depends on the complex vector constant C_{lm} that relates to a given coil geometry and placement:

$$C_{lm} = \oint_{Coil} \frac{Y^*_{lm}(\theta', \phi')}{(2l+1){r'}^{l+1}} \boldsymbol{dI}' = C^x_{lm}\hat{\mathrm{i}} + C^y_{lm}\hat{\mathrm{j}} + C^z_{lm}\hat{k} \quad (1)$$

Where * is the complex conjugate; r', θ', ϕ' are radial distance, polar angle, and azimuthal angle of the differential segment of the coil, $Y_{lm}(\theta', \phi')$ are spherical harmonic functions; I is the current in the coil; $\boldsymbol{dI}'$ is the orientation of the current in the coil along the current path. Further we define D_{lm}, E_{lm}, and F_{lm} to simplify the equations:

$$D_{lm} = \frac{C^x_{lm} - jC^y_{lm}}{2} \quad (2)$$

$$E_{lm} = \frac{C^x_{lm} + jC^y_{lm}}{2} \quad (3)$$

$$\begin{aligned} F_{lm} &= \frac{-j\omega\mu_0 I\left[\sigma_s + j\omega\left(\varepsilon_s - \varepsilon_0\right)\right]}{l\left(\sigma_s + j\omega\varepsilon_s\right) + j\omega\varepsilon_0(l+1)} \\ &\times \left\{-D_{l-1,m-1}\sqrt{\frac{(l+m-1)(l+m)}{(2l+1)(2l-1)}} + E_{l-1,m+1}\sqrt{\frac{(l-m-1)(l-m)}{(2l+1)(2l-1)}}\right. \\ &\left. + C^z_{l-1,m}\sqrt{\frac{(l-m)(l+m)}{(2l+1)(2l-1)}}\right\} \\ &For\ l > 0, \quad F_{00} = 0 \end{aligned} \quad (4)$$

We assume that the sphere has the permeability of free space μ_0, where ε_s and σ_s are the permittivity and conductivity of the homogenous isotropic sphere, respectively. We used $\varepsilon_s \approx 13000\varepsilon_0$ and $\sigma_s = 0.14\ Sm^{-1}$. Using the equations above, the electric field at any given point in space (r, θ, ϕ) along three spherical axes is:

$$\begin{aligned} \boldsymbol{E} \cdot \hat{\boldsymbol{r}} &= -\mu_0 I \sum_{l=1}^{N+1} \sum_{m=-l}^{l} \frac{(j\omega)^2\varepsilon_0(2l+1)}{j\omega\left(\varepsilon_s l + \varepsilon_0 l + \varepsilon_0\right)} r^{l-1} Y_{lm}(\theta, \phi) \\ &\times \left\{-D_{l-1,m-1}\sqrt{\frac{(l+m-1)(l+m)}{(2l+1)(2l-1)}} + E_{l-1,m+1}\sqrt{\frac{(l-m-1)(l-m)}{(2l+1)(2l-1)}}\right. \\ &\left. + C^z_{l-1,m}\sqrt{\frac{(l-m)(l+m)}{(2l+1)(2l-1)}}\right\} \end{aligned} \quad (5)$$

$$
\boldsymbol{E}\cdot\widehat{\boldsymbol{\phi}} = -j\omega\mu_0 I\sum_{l=0}^{N}\sum_{m=-l}^{l} j\times\left(D_{lm}e^{j\phi} - E_{lm}e^{-j\phi}\right)r^{l}Y_{lm}(\theta,\phi) \quad (6)
$$
$$
-\sum_{l=1}^{N+1}\sum_{m=-l}^{l} F_{lm}\frac{jm}{\sin\theta}r^{l-1}Y_{lm}(\theta,\phi)
$$

$$
\begin{aligned}
\boldsymbol{E}\cdot\widehat{\boldsymbol{\theta}} = {} & -j\omega\mu_0 I\sum_{l=0}^{N-1}\sum_{m=-l}^{l}\left\{-C_{l+1,m-1}^{z}\times e^{-j\phi}\sqrt{\frac{(l-m+2)(l-m+1)}{(2l+1)(2l+3)}}\right. \\
& \left.+\sqrt{\frac{(l-m+1)(l+m+1)}{(2l+1)(2l+3)}}\times\left[D_{l+1,m}e^{j\phi}+E_{l+1,m}e^{-j\phi}\right]\right\}r^{l+1}Y_{lm}(\theta,\phi) \\
& -\sum_{l=1}^{N+1}\sum_{m=-l}^{l}\left\{j\omega\mu_0 I\left[C_{l-1,m-1}^{z}e^{-j\phi}\sqrt{\frac{(l+m-1)(l+m)}{(2l-1)(2l+1)}}\right.\right. \\
& \left.+\sqrt{\frac{(l-m)(l+m)}{(2l-1)(2l+1)}}\left(D_{l-1,m}e^{j\phi}+E_{l-1,m}e^{-j\phi}\right)\right]+\frac{1}{2}F_{l,m-1}e^{-j\phi}\sqrt{(l-m-1)(l+m)} \\
& \left.-\frac{1}{2}F_{l,m+1}e^{j\phi}\sqrt{(l+m+1)(l-m)}\right\}r^{l-1}Y_{lm}(\theta,\phi)
\end{aligned} \quad (7)
$$

Equations 5–7 are N^{th} order approximations of the analytical solution. The result converges to the exact solution with $N\to\infty$. In our calculations, we used N = 20 which gives sufficient accuracy based on the convergence rate. In what follows, we define C_{lm} for a one wire loop figure-8 coil (Figure B1).

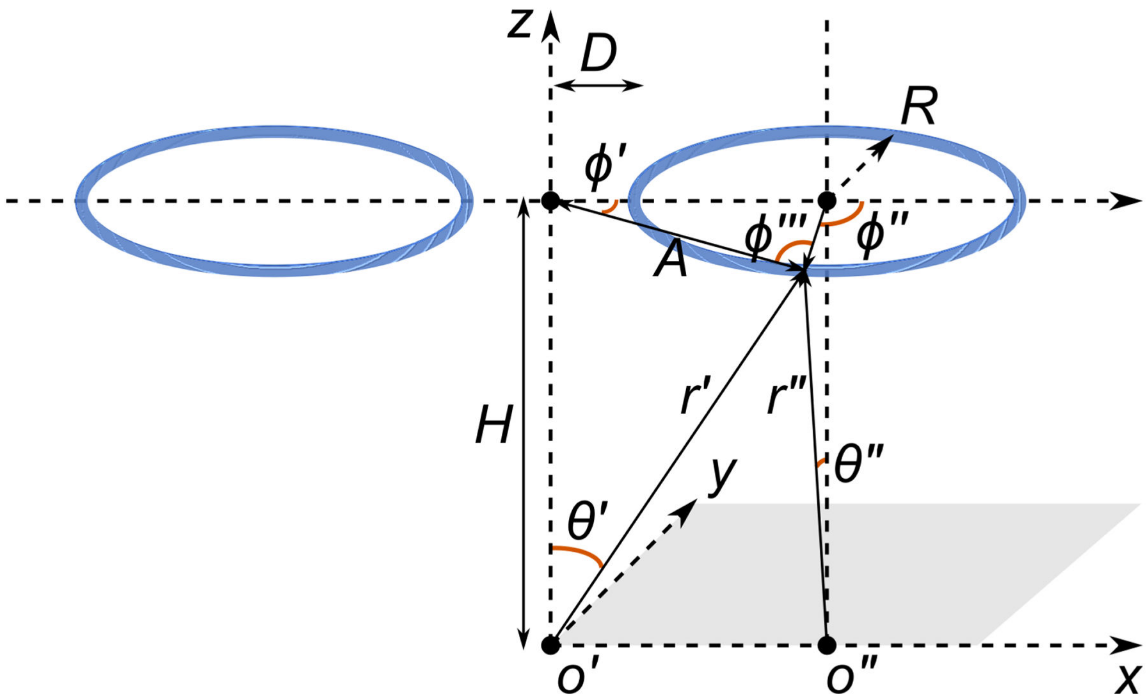

Figure B1.
One wire loop figure-8 coil in a spherical coordinate system.

The one wire figure-8 coil consists of two loops, each with radius R that are parallel to the x-y plane, with the loops along the x-axis, and the center of the coil being a distance H (in our case, 7 mm) above the head. Both loops have a distance D from z-axis. C_{lm} is calculated for each loop separately. For the loop on the positive side of the x-axis, to simplify the calculations, we translated the coordinate system in such way that the center of the loop is directly above the new center of the coordinate system. The old coordinate system relates to the new coordinate system as follows.

Since the sum of the angles in a triangle is π radians,

$$\phi''' = \phi'' - \phi' \quad (8)$$

Using the law of sines in triangles, we have:

$$\frac{\sin \phi'}{R} = \frac{\sin \phi'''}{D+R} = \frac{\sin(\phi'' - \phi')}{D+R} = \frac{\sin \phi'' \cos \phi' - \cos \phi'' \sin \phi'}{D+R} \quad (9)$$

And by simplification we get:

$$\phi' = \tan^{-1}\left(\frac{R \sin \phi''}{D + R + R \cos \phi''}\right) \quad (10)$$

According to the law of cosines in triangles, we have:

$$A = \sqrt{(D+R)^2 + R^2 - 2(D+R)Rcos(\pi - \phi'')}$$

Therefore,

$$\theta' = \tan^{-1}\left(\frac{A}{H}\right) = tan^{-1}\left(\frac{\sqrt{(D+R)^2 + R^2 - 2(D+R)Rcos(\pi - \phi'')}}{H}\right) \quad (12)$$

$$r' = \sqrt{H^2 + A^2} = \sqrt{H^2 + (D+R)^2 + R^2 - 2(D+R)Rcos(\pi - \phi'')} \quad (13)$$

Given such coordinate translation and assuming a counterclockwise direction for the loop current, the integral can be written as:

$$C_{lm} = \oint_{coil} \frac{Y_{lm}^{*}(\theta', \phi')}{(2l+1)r'^{l+1}} \boldsymbol{dI'} = \int_{\phi'' = -\pi}^{\pi} G_{lm}(\phi'') \boldsymbol{dI'} \quad (14)$$

Where

$$G_{lm}(\phi'') = \frac{Y_{lm}^{*}\left(tan^{-1}\left(\frac{\sqrt{(D+R)^2 + R^2 - 2(D+R)Rcos(\pi - \phi'')}}{H}\right), \tan^{-1}\left(\frac{R \sin \phi''}{D + R + R \cos \phi''}\right)\right)}{(2l+1)\left(\sqrt{H^2 + (D+R)^2 + R^2 - 2(D+R)Rcos(\pi - \phi'')}\right)^{l+1}} \quad (15)$$

Therefore, by expanding the integral over x, y and z orientations, we arrive at:

$$C_{lm} = C_{lm}^{x}\,\hat{\imath} + C_{lm}^{y}\,\hat{\jmath} + C_{lm}^{z}\,\hat{k}$$

Additionally, we know that in the old coordinate system

$$x = D + Rcos(\phi''), \quad y = Rsin(\phi''), \quad z = H$$

Then,

$$C_{lm}^{x} = \int_{\phi'' = -\pi}^{\pi} G_{lm}(\phi'')dx = \int_{\phi'' = -\pi}^{\pi} -G_{lm}(\phi'')Rsin(\phi'')d\phi'' \quad (16)$$

$$C_{lm}^{y} = \int_{\phi'' = -\pi}^{\pi} G_{lm}(\phi'')dy = \int_{\phi'' = -\pi}^{\pi} G_{lm}(\phi'')Rcos(\phi'')d\phi'' \quad (17)$$

$$C_{lm}^{z} = \int_{\phi'' = -\pi}^{\pi} G_{lm}(\phi'')dz'' = 0 \quad (18)$$

All the above steps can be repeated for the other loop with the opposite current direction. The only change in equations (15–17) will be:

$$G_{lm}(\phi'') = \frac{Y_{lm}^{*}\left(tan^{-1}\left(\frac{\sqrt{(D+R)^2 + R^2 - 2(D+R)Rcos(\pi - \phi'')}}{H}\right), \pi + \tan^{-1}\left(\frac{R \sin \phi''}{D + R + R \cos \phi''}\right)\right)}{(2l+1)\left(\sqrt{H^2 + (D+R)^2 + R^2 - 2(D+R)Rcos(\pi - \phi'')}\right)^{l+1}} \quad (19)$$

Finally, both integral results are added together to calculate C_{lm} for the whole one wire figure-8 coil. However, the real coils often have multiple wire bindings. We implemented a coil with 9 nested concentric loops, which were added together, according to the same specifications as for the numeric simulations.

References

Aberra AS, Wang B, Grill WM, Peterchev AV, 2018 Simulation of transcranial magnetic stimulation in head model with morphologically-realistic cortical neurons. bioRxiv. 10.1101/506204

Alekseichuk I, Falchier AY, Linn G, Xu T, Milham MP, Schroeder CE, Opitz A, 2018 Electric Field Dynamics In The Brain During Multi-Electrode Transcranial Electric Stimulation. bioRxiv. 10.1101/340224

Allen JS, Damasio H, Grabowski TJ, 2002 Normal neuroanatomical variation in the human brain: An MRI-volumetric study. Am. J. Phys. Anthropol 118, 341–358. 10.1002/ajpa.10092 [PubMed: 12124914]

Antal A, Alekseichuk I, Bikson M, Brockmöller J, Brunoni A, Chen R, Cohen LG, Dowthwaite G, Ellrich J, Flöel A, Fregni F, George MS, Hamilton R, Haueisen J, Herrmann CS, Hummel F, Lefaucheur JP, Liebetanz D, Loo CK, McCaig CD, Miniussi C, Miranda PC, Moliadze V, Nitsche MA, Nowak R, Padberg F, Pascual-Leone A, Poppendieck W, Priori A, Rossi S, Rossini PM, Rothwell J, Rueger MA, Ruffini G, Schellhorn K, Siebner HR, Ugawa Y, Wexler A, Ziemann U, Hallett M, Paulus W, 2017 Low intensity transcranial electric stimulation: Safety, ethical, legal regulatory and application guidelines. Clin. Neurophysiol 128, 1774–1809. 10.1016/j.clinph.2017.06.001 [PubMed: 28709880]

Aspart F, Remme MWH, Obermayer K, 2018 Differential polarization of cortical pyramidal neuron dendrites through weak extracellular fields. PLOS Comput. Biol 14, e1006124 10.1371/journal.pcbi.1006124 [PubMed: 29727454]

Attene M, 2010 A lightweight approach to repairing digitized polygon meshes. Vis. Comput 26, 1393–1406. 10.1007/s00371-010-0416-3

Balslev D, Braet W, McAllister C, Miall RC, 2007 Inter-individual variability in optimal current direction for transcranial magnetic stimulation of the motor cortex. J. Neurosci. Methods 162, 309–313. 10.1016/j.jneumeth.2007.01.021 [PubMed: 17353054]

Barnes WL, Lee Won Hee, Peterchev AV, 2014 Approximating transcranial magnetic stimulation with electric stimulation in mouse: A simulation study, in: 2014 36th Annual International Conference of the IEEE Engineering in Medicine and Biology Society IEEE, pp. 6129–6132. 10.1109/EMBC.2014.6945028

Bernabei JM, Lee Won Hee, Peterchev AV, 2014 Modeling transcranial electric stimulation in mouse: A high resolution finite element study, in: 2014 36th Annual International Conference of the IEEE Engineering in Medicine and Biology Society IEEE, pp. 406–409. 10.1109/EMBC.2014.6943614

Brasil-Neto JP, Cohen LG, Panizza M, Nilsson J, Roth BJ, Hallett M, 1992 Optimal focal transcranial magnetic activation of the human motor cortex: effects of coil orientation, shape of the induced current pulse, and stimulus intensity. J. Clin. Neurophysiol 9, 132–136. [PubMed: 1552001]

Cambiaghi M, Teneud L, Velikova S, Gonzalez-Rosa JJ, Cursi M, Comi G, Leocani L, 2011 Flash visual evoked potentials in mice can be modulated by transcranial direct current stimulation. Neuroscience 185, 161–165. 10.1016/j.neuroscience.2011.04.022 [PubMed: 21515340]

Crowther LJ, Hadimani RL, Kanthasamy AG, Jiles DC, 2014 Transcranial magnetic stimulation of mouse brain using high-resolution anatomical models. J. Appl. Phys 115, 17B303 10.1063/1.4862217

Datta A, Bansal V, Diaz J, Patel J, Reato D, Bikson M, 2009 Gyri-precise head model of transcranial direct current stimulation: Improved spatial focality using a ring electrode versus conventional rectangular pad. Brain Stimul. 2, 201–207.e1. 10.1016/j.brs.2009.03.005 [PubMed: 20648973]

Deng Z-D, Lisanby SH, Peterchev AV, 2013 Electric field depth–focality tradeoff in transcranial magnetic stimulation: Simulation comparison of 50 coil designs. Brain Stimul. 6, 1–13. 10.1016/j.brs.2012.02.005 [PubMed: 22483681]

Dogdas B, Stout D, Chatziioannou AF, Leahy RM, 2007 Digimouse: a 3D whole body mouse atlas from CT and cryosection data. Phys. Med. Biol 52, 577–587. 10.1088/0031-9155/52/3/003 [PubMed: 17228106]

Eaton H, 1992 Electric field induced in a spherical volume conductor from arbitrary coils: application to magnetic stimulation and MEG. Med. Biol. Eng. Comput 30, 433–40. 10.1007/BF02446182 [PubMed: 1487945]

Faraji J, Gomez-Palacio-Schjetnan A, Luczak A, Metz GA, 2013 Beyond the silence: Bilateral somatosensory stimulation enhances skilled movement quality and neural density in intact behaving rats. Behav. Brain Res. 253, 78–89. 10.1016/j.bbr.2013.07.022 [PubMed: 23871611]

Fischl B, 2012 FreeSurfer. Neuroimage 62, 774–781. 10.1016/j.neuroimage.2012.01.021 [PubMed: 22248573]

Geuzaine C, 2007 GetDP: a general finite-element solver for the de Rham complex. PAMM 7, 1010603–1010604. 10.1002/pamm.200700750

Geuzaine C, Remacle J-F, 2009 Gmsh: A 3-D finite element mesh generator with built-in pre- and post-processing facilities. Int. J. Numer. Methods Eng. 79, 1309–1331. 10.1002/nme.2579

Grossman N, Bono D, Dedic N, Kodandaramaiah SB, Rudenko A, Suk H-J, Cassara AM, Neufeld E, Kuster N, Tsai L-H, Pascual-Leone A, Boyden ES, 2017 Noninvasive Deep Brain Stimulation via Temporally Interfering Electric Fields. Cell 169, 1029–1041. 10.1016/j.cell.2017.05.024 [PubMed: 28575667]

Grossman P, Alekseichuk I, de Lara G, Paneri K, Kunz P, Turi Z, Bikson M, Paulus W, Antal A, 2018 transcranial Direct Current Stimulation Studies Open Database (tDCS-OD). bioRxiv. 10.1101/369215

Hammelrath L, Škokić S, Khmelinskii A, Hess A, van der Knaap N, Staring M, Lelieveldt BPF, Wiedermann D, Hoehn M, 2016 Morphological maturation of the mouse brain: An in vivo MRI and histology investigation. Neuroimage 125, 144–152. 10.1016/j.neuroimage.2015.10.009 [PubMed: 26458518]

Hoppenrath K, Funke K, 2013 Time-course of changes in neuronal activity markers following iTBS-TMS of the rat neocortex. Neurosci. Lett 536, 19–23. 10.1016/j.neulet.2013.01.003 [PubMed: 23328445]

Huang Y, Liu AA, Lafon B, Friedman D, Dayan M, Wang X, Bikson M, Doyle WK, Devinsky O, Parra LC, 2017 Measurements and models of electric fields in the in vivo human brain during transcranial electric stimulation. Elife 6, e18834 10.7554/eLife.18834 [PubMed: 28169833]

Isler K, Christopher Kirk E, Miller JMA, Albrecht GA, Gelvin BR, Martin RD, 2008 Endocranial volumes of primate species: scaling analyses using a comprehensive and reliable data set. J. Hum. Evol 55, 967–978. 10.1016/j.jhevol.2008.08.004 [PubMed: 18817943]

Jenkinson M, Beckmann CF, Behrens TEJ, Woolrich MW, Smith SM, 2012 FSL. Neuroimage 62, 782–790. 10.1016/j.neuroimage.2011.09.015 [PubMed: 21979382]

Kar K, Duijnhouwer J, Krekelberg B, 2017 Transcranial Alternating Current Stimulation Attenuates Neuronal Adaptation. J. Neurosci 37, 2325–2335. 10.1523/JNEUROSCI.2266-16.2016 [PubMed: 28137971]

Krause MR, Zanos TP, Csorba BA, Pilly PK, Choe J, Phillips ME, Datta A, Pack CC, 2017 Transcranial Direct Current Stimulation Facilitates Associative Learning and Alters Functional Connectivity in the Primate Brain. Curr. Biol 27, 3086–3096.e3. 10.1016/j.cub.2017.09.020 [PubMed: 29033331]

Laakso I, Tanaka S, Koyama S, De Santis V, Hirata A, 2015 Inter-subject Variability in Electric Fields of Motor Cortical tDCS. Brain Stimul. 8, 906–913. 10.1016/j.brs.2015.05.002 [PubMed: 26026283]

Liebetanz D, Klinker F, Hering D, Koch R, Nitsche MA, Potschka H, Loscher W, Paulus W, Tergau F, 2006 Anticonvulsant Effects of Transcranial Direct-current Stimulation (tDCS) in the Rat Cortical Ramp Model of Focal Epilepsy. Epilepsia 47, 1216–1224. 10.1111/j.1528-1167.2006.00539.x [PubMed: 16886986]

Liu A, Vöröslakos M, Kronberg G, Henin S, Krause MR, Huang Y, Opitz A, Mehta A, Pack CC, Krekelberg B, Berényi A, Parra LC, Melloni L, Devinsky O, Buzsáki G, 2018 Immediate neurophysiological effects of transcranial electrical stimulation. Nat. Commun 9, 5092 10.1038/s41467-018-07233-7 [PubMed: 30504921]

Miranda PC, Callejón-Leblic MA, Salvador R, Ruffini G, 2018 Realistic modeling of transcranial current stimulation: The electric field in the brain. Curr. Opin. Biomed. Eng 8, 20–27. 10.1016/j.cobme.2018.09.002

Miranda PC, Mekonnen A, Salvador R, Ruffini G, 2013 The electric field in the cortex during transcranial current stimulation. Neuroimage 70, 48–58. 10.1016/j.neuroimage.2012.12.034 [PubMed: 23274187]

Monai H, Ohkura M, Tanaka M, Oe Y, Konno A, Hirai H, Mikoshiba K, Itohara S, Nakai J, Iwai Y, Hirase H, 2016 Calcium imaging reveals glial involvement in transcranial direct current stimulation-induced plasticity in mouse brain. Nat. Commun 7, 11100 10.1038/ncomms11100 [PubMed: 27000523]

Mueller JK, Grigsby EM, Prevosto V, Petraglia FW, Rao H, Deng Z-D, Peterchev AV, Sommer MA, Egner T, Platt ML, Grill WM, 2014 Simultaneous transcranial magnetic stimulation and single-neuron recording in alert non-human primates. Nat. Neurosci 17, 1130–1136. 10.1038/nn.3751 [PubMed: 24974797]

Nielsen JD, Madsen KH, Puonti O, Siebner HR, Bauer C, Madsen CG, Saturnino GB, Thielscher A, 2018 Automatic skull segmentation from MR images for realistic volume conductor models of the head: Assessment of the state-of-the-art. Neuroimage 174, 587–598. 10.1016/j.neuroimage.2018.03.001 [PubMed: 29518567]

Nitsche MA, Bikson M, 2017 Extending the parameter range for tDCS: Safety and tolerability of 4 mA stimulation. Brain Stimul. 10, 541–542. 10.1016/j.brs.2017.03.002 [PubMed: 28456325]

Opitz A, Falchier A, Linn GS, Milham MP, Schroeder CE, 2017 Limitations of ex vivo measurements for in vivo neuroscience. Proc. Natl. Acad. Sci 114, 5243–5246. 10.1073/pnas.1617024114 [PubMed: 28461475]

Opitz A, Falchier A, Yan C, Yeagle EM, Linn GS, Megevand P, Thielscher A, Deborah A,R, Milham MP, Mehta AD, Schroeder CE, 2016 Spatiotemporal structure of intracranial electric fields induced by transcranial electric stimulation in humans and nonhuman primates. Sci. Rep 6, 31236 10.1038/srep31236 [PubMed: 27535462]

Opitz A, Legon W, Rowlands A, Bickel WK, Paulus W, Tyler WJ, 2013 Physiological observations validate finite element models for estimating subject-specific electric field distributions induced by transcranial magnetic stimulation of the human motor cortex. Neuroimage 81, 253–264. 10.1016/j.neuroimage.2013.04.067 [PubMed: 23644000]

Opitz A, Paulus W, Will S, Antunes A, Thielscher A, 2015 Determinants of the electric field during transcranial direct current stimulation. Neuroimage 109, 140–150. 10.1016/j.neuroimage.2015.01.033 [PubMed: 25613437]

Opitz A, Windhoff M, Heidemann RM, Turner R, Thielscher A, 2011 How the brain tissue shapes the electric field induced by transcranial magnetic stimulation. Neuroimage 58, 849–859. 10.1016/j.neuroimage.2011.06.069 [PubMed: 21749927]

Opitz A, Yeagle E, Thielscher A, Schroeder C, Mehta AD, Milham MP, 2018 On the importance of precise electrode placement for targeted transcranial electric stimulation. Neuroimage 181, 560–567. 10.1016/j.neuroimage.2018.07.027 [PubMed: 30010008]

Parthoens J, Verhaeghe J, Servaes S, Miranda A, Stroobants S, Staelens S, 2016 Performance Characterization of an Actively Cooled Repetitive Transcranial Magnetic Stimulation Coil for the Rat. Neuromodulation Technol. Neural Interface 19, 459–468. 10.1111/ner.12387

Pasley BN, Allen EA, Freeman RD, 2009 State-Dependent Variability of Neuronal Responses to Transcranial Magnetic Stimulation of the Visual Cortex. Neuron 62, 291–303. 10.1016/j.neuron.2009.03.012 [PubMed: 19409273]

Paulus W, Nitsche MA, Antal A, 2016 Application of Transcranial Electric Stimulation (tDCS, tACS, tRNS). Eur. Psychol 21, 4–14. 10.1027/1016-9040/a000242

Pedron S, Monnin J, Haffen E, Sechter D, Van Waes V, 2014 Repeated Transcranial Direct Current Stimulation Prevents Abnormal Behaviors Associated with Abstinence from Chronic Nicotine Consumption. Neuropsychopharmacology 39, 981–988. 10.1038/npp.2013.298 [PubMed: 24154668]

Peterchev AV, Rosa MA, Deng Z-D, Prudic J, Lisanby SH, 2010 Electroconvulsive Therapy Stimulus Parameters. J. ECT 26, 159–174. 10.1097/YCT.0b013e3181e48165 [PubMed: 20805726]

Peterchev AV, Wagner TA, Miranda PC, Nitsche MA, Paulus W, Lisanby SH, Pascual-Leone A, Bikson M, 2012 Fundamentals of transcranial electric and magnetic stimulation dose: Definition, selection, and reporting practices. Brain Stimul. 5, 435–453. 10.1016/j.brs.2011.10.001 [PubMed: 22305345]

Polanía R, Nitsche MA, Ruff CC, 2018 Studying and modifying brain function with non-invasive brain stimulation. Nat. Neurosci 21, 174–187. 10.1038/s41593-017-0054-4 [PubMed: 29311747]

Radman T, Ramos RL, Brumberg JC, Bikson M, 2009 Role of cortical cell type and morphology in subthreshold and suprathreshold uniform electric field stimulation in vitro. Brain Stimul. 2, 215–228.e3. 10.1016/j.brs.2009.03.007 [PubMed: 20161507]

Rawji V, Ciocca M, Zacharia A, Soares D, Truong D, Bikson M, Rothwell J, Bestmann S, 2018 tDCS changes in motor excitability are specific to orientation of current flow. Brain Stimul. 11, 289–298. 10.1016/j.brs.2017.11.001 [PubMed: 29146468]

Reveley C, Gruslys A, Ye FQ, Glen D, Samaha J, E. Russ B, Saad Z, K. Seth A, Leopold DA, Saleem KS, 2016 Three-Dimensional Digital Template Atlas of the Macaque Brain. Cereb. Cortex 27, 4463–4477. 10.1093/cercor/bhw248

Richter L, Neumann G, Oung S, Schweikard A, Trillenberg P, 2013 Optimal Coil Orientation for Transcranial Magnetic Stimulation. PLoS One 8, e60358 10.1371/journal.pone.0060358 [PubMed: 23593200]

Rossi S, Hallett M, Rossini PM, Pascual-Leone A, 2009 Safety, ethical considerations, and application guidelines for the use of transcranial magnetic stimulation in clinical practice and research. Clin. Neurophysiol 120, 2008–2039. 10.1016/j.clinph.2009.08.016 [PubMed: 19833552]

Salvador R, Miranda PC, 2009 Transcranial magnetic stimulation of small animals: A modeling study of the influence of coil geometry, size and orientation. Proc. 31st Annu. Int. Conf. IEEE Eng. Med. Biol. Soc. Eng. Futur. Biomed. EMBC 2009 674–677. 10.1109/IEMBS.2009.5334070

Seo H, Jun SC, 2019 Relation between the electric field and activation of cortical neurons in transcranial electrical stimulation. Brain Stimul. 12, 275–289. 10.1016/j.brs.2018.11.004 [PubMed: 30449635]

Seo H, Jun SC, 2017 Multi-Scale Computational Models for Electrical Brain Stimulation. Front. Hum. Neurosci 11 10.3389/fnhum.2017.00515

Takano Y, Yokawa T, Masuda A, Niimi J, Tanaka S, Hironaka N, 2011 A rat model for measuring the effectiveness of transcranial direct current stimulation using fMRI. Neurosci. Lett 491, 40–43. 10.1016/j.neulet.2011.01.004 [PubMed: 21215288]

Terzuolo CA, Bullock TH, 1956 Measurement of imposed voltage gradient adequate to modulate neuronal firing. Proc. Natl. Acad. Sci 42, 687–694. 10.1073/pnas.42.9.687 [PubMed: 16589932]

Thielscher A, Kammer T, 2004 Electric field properties of two commercial figure-8 coils in TMS: calculation of focality and efficiency. Clin. Neurophysiol 115, 1697–1708. 10.1016/j.clinph.2004.02.019 [PubMed: 15203072]

Thielscher A, Kammer T, 2002 Linking Physics with Physiology in TMS: A Sphere Field Model to Determine the Cortical Stimulation Site in TMS. Neuroimage 17, 1117–1130. 10.1006/nimg.2002.1282 [PubMed: 12414254]

Thielscher A, Opitz A, Windhoff M, 2011 Impact of the gyral geometry on the electric field induced by transcranial magnetic stimulation. Neuroimage 54, 234–243. 10.1016/j.neuroimage.2010.07.061 [PubMed: 20682353]

Valero-Cabré A, Amengual JL, Stengel C, Pascual-Leone A, Coubard OA, 2017 Transcranial magnetic stimulation in basic and clinical neuroscience: A comprehensive review of fundamental principles and novel insights. Neurosci. Biobehav. Rev 83, 381–404. 10.1016/j.neubiorev.2017.10.006 [PubMed: 29032089]

Vöröslakos M, Takeuchi Y, Brinyiczki K, Zombori T, Oliva A, Fernández-Ruiz A, Kozák G, Kincses ZT, Iványi B, Buzsáki G, Berényi A, 2018 Direct effects of transcranial electric stimulation on brain circuits in rats and humans. Nat. Commun 9, 483 10.1038/s41467-018-02928-3 [PubMed: 29396478]

Wachter D, Wrede A, Schulz-Schaeffer W, Taghizadeh-Waghefi A, Nitsche MA, Kutschenko A, Rohde V, Liebetanz D, 2011 Transcranial direct current stimulation induces polarity-specific changes of cortical blood perfusion in the rat. Exp. Neurol 227, 322–327. 10.1016/j.expneurol.2010.12.005 [PubMed: 21147105]

Wagner S, Rampersad SM, Aydin Ü, Vorwerk J, Oostendorp TF, Neuling T, Herrmann CS, Stegeman DF, Wolters CH, 2014 Investigation of tDCS volume conduction effects in a highly realistic head model. J. Neural Eng. 11, 016002 10.1088/1741-2560/11/1/016002 [PubMed: 24310982]

Wagner TA, Zahn M, Grodzinsky AJ, Pascual-Leone A, 2004 Three-Dimensional Head Model Simulation of Transcranial Magnetic Stimulation. IEEE Trans. Biomed. Eng 51, 1586–1598. 10.1109/TBME.2004.827925 [PubMed: 15376507]

Weissman JD, Epstein CM, Davey KR, 1992 Magnetic brain stimulation and brain size: relevance to animal studies. Electroencephalogr. Clin. Neurophysiol 85, 215–219. 10.1016/0168-5597(92)90135-X [PubMed: 1376680]

Windhoff M, Opitz A, Thielscher A, 2013 Electric field calculations in brain stimulation based on finite elements: An optimized processing pipeline for the generation and usage of accurate individual head models. Hum. Brain Mapp. 34, 923–935. 10.1002/hbm.21479 [PubMed: 22109746]

Yushkevich PA, Piven J, Hazlett HC, Smith RG, Ho S, Gee JC, Gerig G, 2006 User-guided 3D active contour segmentation of anatomical structures: Significantly improved efficiency and reliability. Neuroimage 31, 1116–1128. 10.1016/j.neuroimage.2006.01.015 [PubMed: 16545965]

HIGHLIGHTS

- Translational research in brain stimulation should account for large differences in induced electric fields in different organisms
- We simulate TMS and TES electric fields using anatomically realistic finite element models in three species: mouse, monkey, and human
- TMS with a 70 mm figure-8 coil creates an approximately 2-times weaker electric field in a mouse brain than in monkey and human brains, where electric field strength is comparable
- Two-electrode TES creates an approximately 100-times stronger electric field in a mouse brain and 3.5-times stronger electric field in a monkey brain than in a human brain

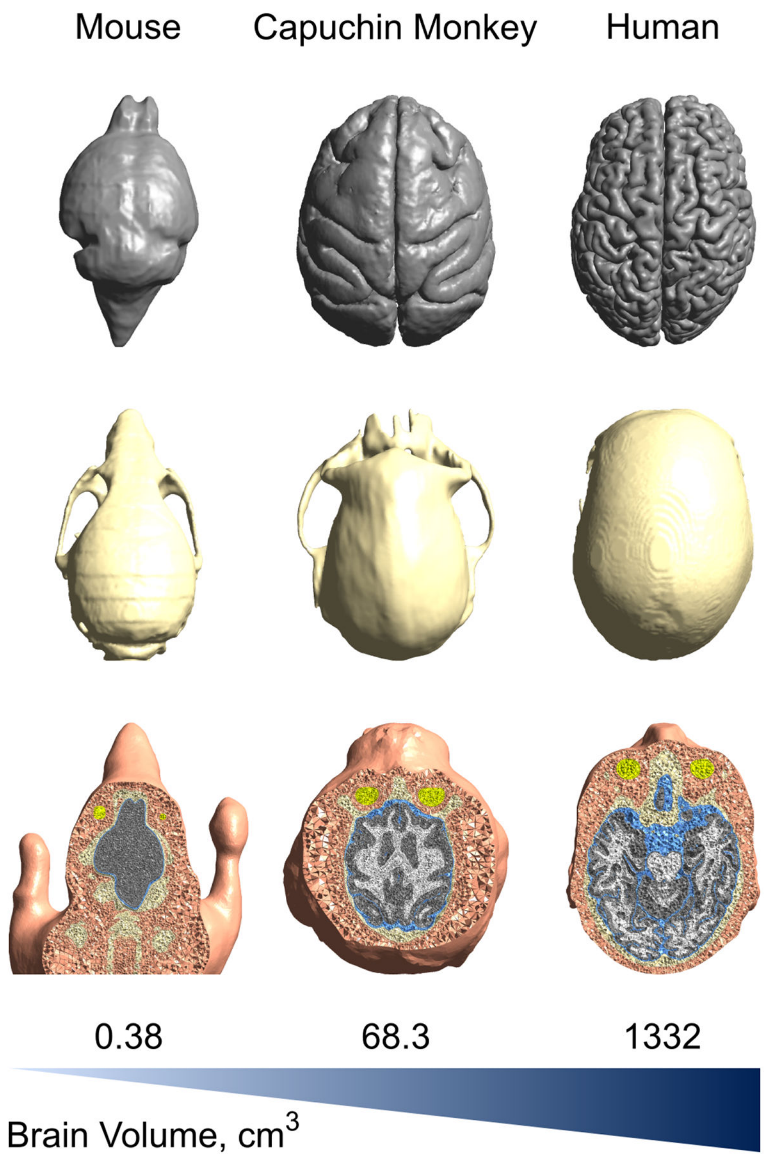

Figure 1.
Anatomically accurate FEM models of mouse, monkey, and human. The following tissues are considered: skin and soft tissues, skull and bones, eyes, CSF, grey matter, and white matter. On the top row are the brain surfaces, middle row – skull surfaces, bottom row – horizontal cut of FEMs.

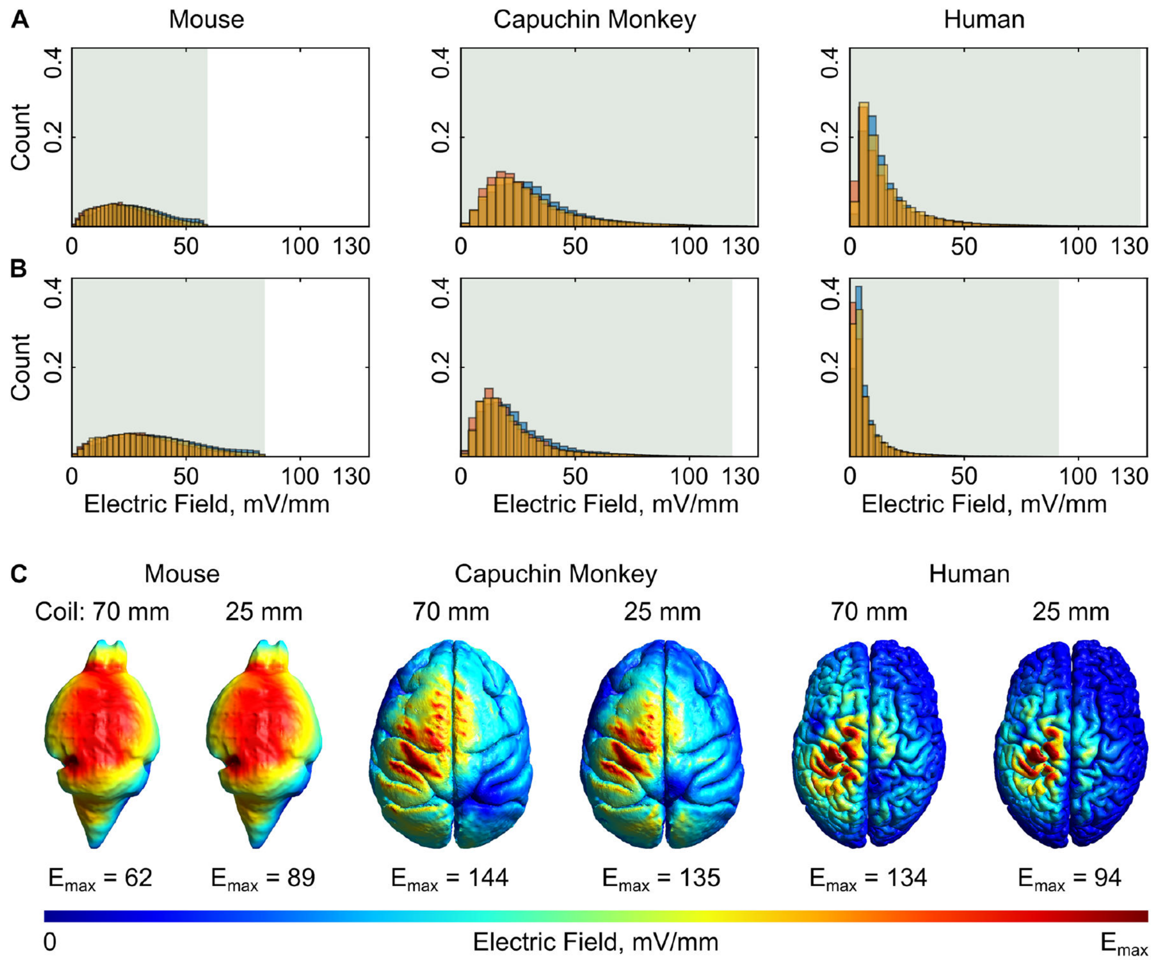

Figure 2.

Distribution of the electric field strength in the grey matter volume for a 70 mm (A) and 25 mm (B) figure-8 coil. Blue color corresponds to the caudal-medial or CM coil orientation, red color – medial or M, and yellow – caudal-lateral or CL coil orientation. The grey zone shows the range of the data on the x-axis. The same plots on the individual axes are shown in Figure S4. (C) Normalized electric fields on the brain surfaces for the CM orientation. See other montages in Figures S1, S2.

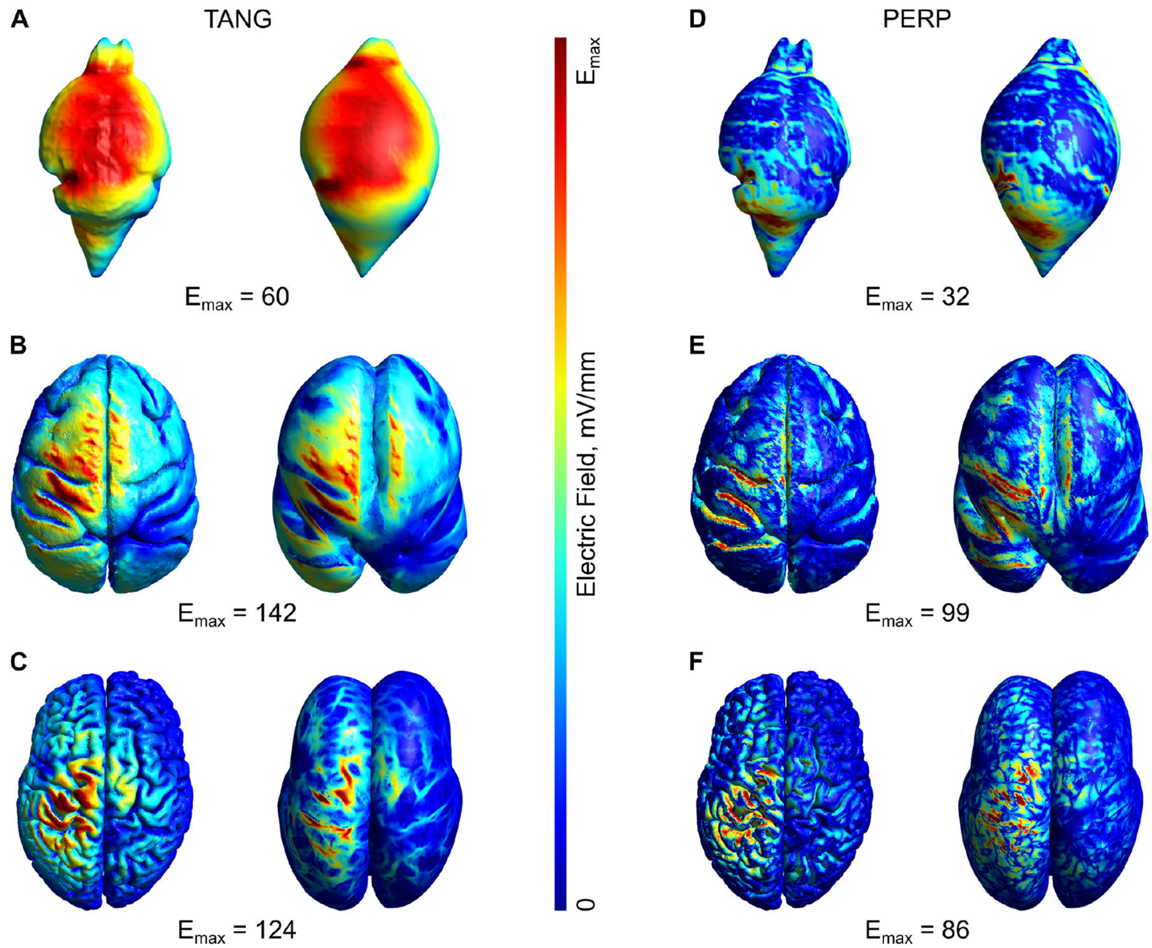

Figure 3.

Distribution of the tangential (A-C) and perpendicular (D-F) components of the electric field for the 70 mm figure-8 coil oriented caudal-medial for mouse (top row), monkey (middle row), and human (bottom row). For each figure in the panel, both the anatomical realistic surface (left) and the inflated surface (right) is shown.

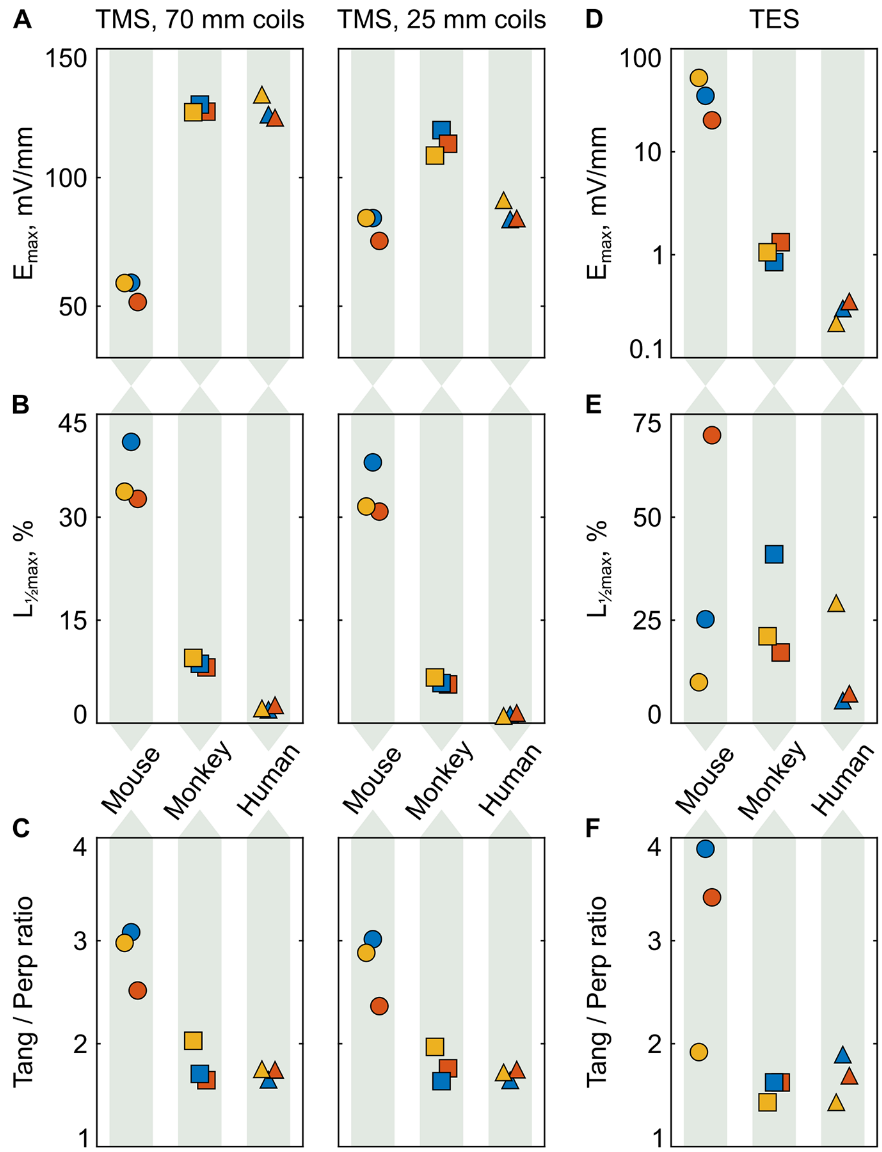

Figure 4.

(A-C) TMS summary statistics across species. Color encodes the coil orientation: blue – caudal-medial, red – medial, and yellow – caudal-lateral. (D-F) TES summary statistics across species. Color encodes the electrode montage: blue – rostral-caudal, red – left-right, and yellow – dorsal-ventral.

The shape of the data points indicates the species: round – mouse, square – monkey, triangle – human. The top row depicts the robust maximum of the electric field (E_{max}), the middle row – the affected brain volume ($L_{½max}$), and the bottom row – the ratio of the medians of the tangential to perpendicular field components.

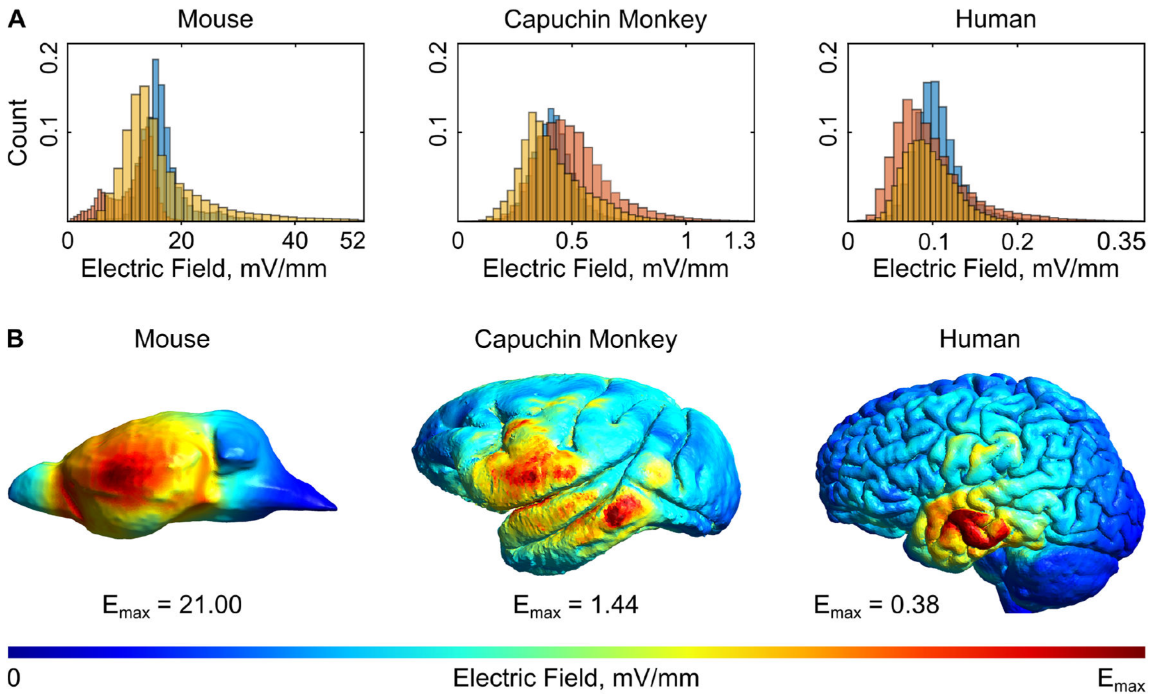

Figure 5.

(A) Distribution of the electric field magnitude in the grey matter volume during TES with the following electrode montages: blue color – rostral-caudal, red – left-right (L-R), and yellow – dorsal-ventral. Note that the x-axes are scaled to the model-specific maximum values. (B) Normalized electric fields on the brain surface for the L-R montage. See the results for the other montages in Figure S3.

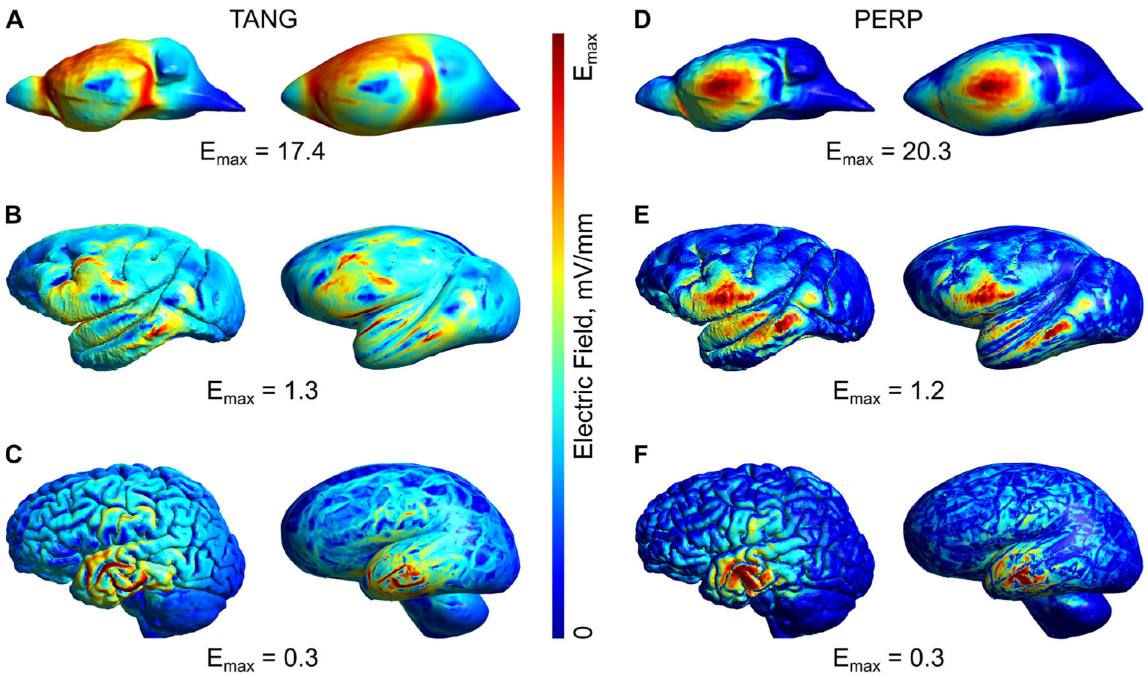

Figure 6.

Distribution of the tangential (A-C) and perpendicular (D-F) components of the electric field on the brain surface due to TES with the left-right electrode montage. On the top row is mouse, middle row – monkey, and bottom row – human. For each figure in the panel, normal surface is on the left and its inflated version is on the right.

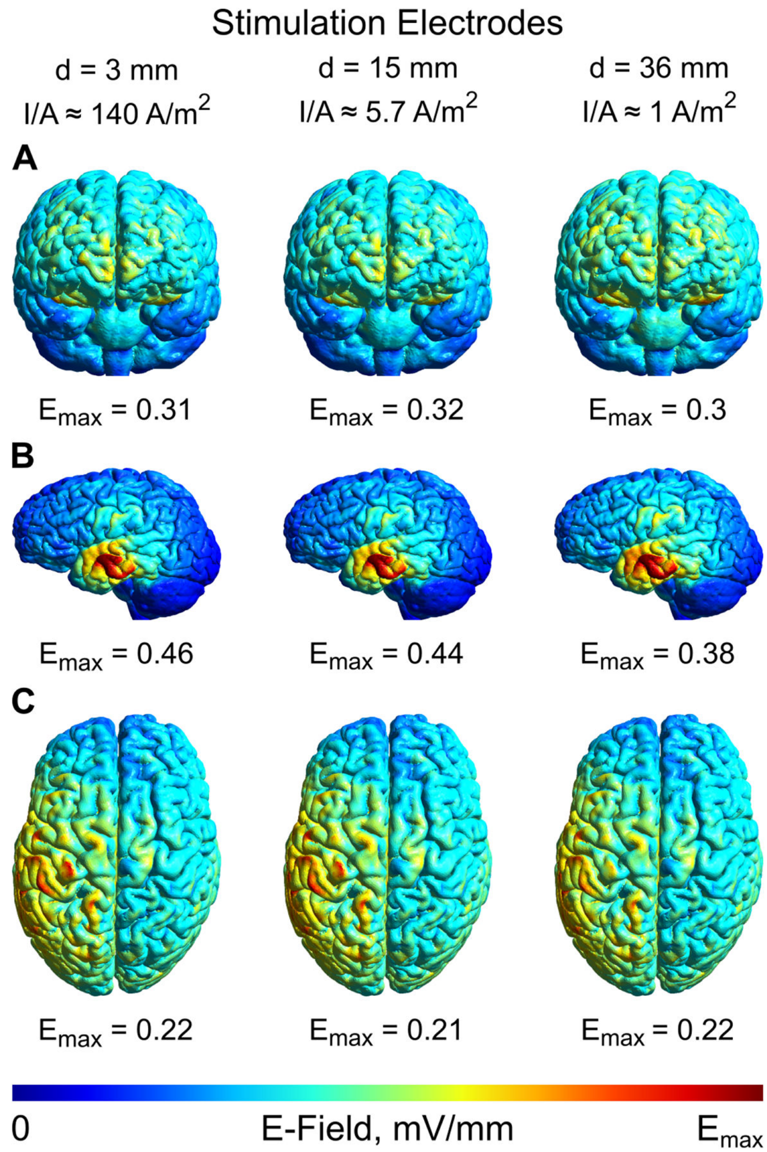

Figure 7.

TES electric fields in grey matter for different sizes of stimulation electrodes (d = 36 mm, 15 mm, and 3 mm). (A) Frontal view for the rostral-caudal electrode montage. (B) Lateral view for the left-right montage. (C) Transverse view for the dorsal-ventral montage.

Table 1.

Summary of the head models. The brain size is given in the following projections: rostral-caudal (RC), left-right (LR), and dorsal-ventral (DV).

Model	Brain Size, cm			Brain Volume, cm^3	Head Volume, cm^3
	RC	LR	DV		
Mouse	1.71	0.94	0.72	0.38	3.10
Capuchin Monkey	6.60	5.50	5.00	68.31	472.66
Macaque Monkey	7.50	5.87	4.59	83.45	505.58
Human	18.55	13.60	12.95	1331.87	5270.54